

***Title Page:***

**Short-term starvation inhibits CD36 N-glycosylation and downregulates USP7 UFMylation to alleviate RBPJ-maintained T cell exhaustion in liver cancer**

Banglun Pan<sup>1#</sup>, Siyan Chen<sup>2#</sup>, Hao Wu<sup>1#</sup>, Xiaoxia Zhang<sup>1</sup>, Zhu Zhang<sup>1</sup>, Dongjie Ye<sup>1</sup>, Yuxin Yao<sup>1</sup>, Yue Luo<sup>1</sup>, Xinyu Zhang<sup>1</sup>, Xiaoqian Wang<sup>1,3</sup>, Nanhong Tang<sup>1,3,4,5\*</sup>

<sup>1</sup>Department of Hepatobiliary Surgery and Fujian Institute of Hepatobiliary Surgery, Fujian Medical University Union Hospital, Fuzhou 350001, China.

<sup>2</sup>Department of Laboratory Medicine, Fujian Medical University Union Hospital, Fuzhou 350001, China.

<sup>3</sup>Cancer Center of Fujian Medical University, Fujian Medical University Union Hospital, Fuzhou 350001, China.

<sup>4</sup>Key Laboratory of Clinical Laboratory Technology for Precision Medicine (Fujian Medical University), Fujian Province University; Fuzhou 350122, China.

<sup>5</sup>Key Laboratory of Ministry of Education for Gastrointestinal Cancer, Fujian Medical University, Fuzhou 350122, China.

<sup>#</sup>These authors contributed equally to this work and shared first authorship.

Corresponding author: Nanhong Tang, Professor, Ph.D., Email: fzttnh@fjmu.edu.cn

23    **Abstract**

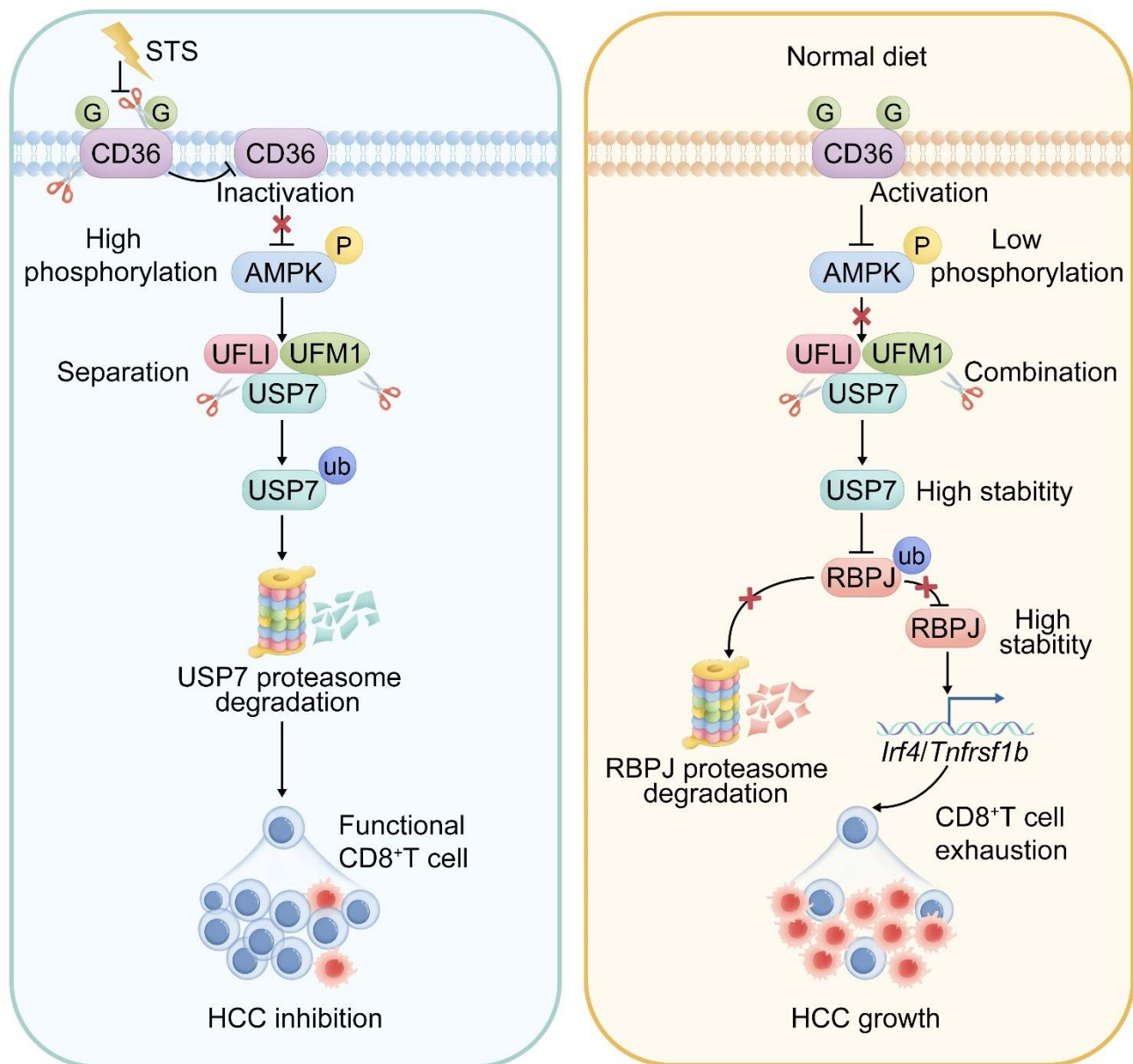
24    **Rationale:** Short-term starvation (STS) has been shown to enhance the sensitivity of tumors to  
25    chemotherapy while concurrently safeguarding normal cells from its detrimental side effects.  
26    Nonetheless, the extent to which STS relies on the anti-tumor immune response to impede the  
27    progression of hepatocellular carcinoma (HCC) remains uncertain.

28    **Methods:** In this study, we employed mass cytometry, flow cytometry, immunoprecipitation,  
29    immunoblotting, CUT&Tag, RT-qPCR, and DNA pull-down assays to evaluate the relationship  
30    between STS and T-cell antitumor immunity in HCC.

31    **Results:** We demonstrated that STS alleviated T cell exhaustion in HCC. This study elucidated the  
32    mechanism by which STS blocked CD36 N-glycosylation, leading to the upregulation of AMPK  
33    phosphorylation and the downregulation of USP7 UFMylation, thus enhancing ubiquitination and  
34    destabilized USP7. Consequently, diminished USP7 levels facilitated the ubiquitination and subsequent  
35    degradation of RBPJ, thereby inhibiting T cell exhaustion through the IRF4/TNFRSF1B axis. From a  
36    therapeutic standpoint, STS not only suppressed the growth of patient-derived orthotopic xenografts  
37    but also enhanced their sensitivity to immunotherapy.

38    **Conclusions:** These findings uncovered a novel mechanism by which N-glycosylation participated in  
39    UFMylation/ubiquitination to regulate T cell exhaustion, and we underscored the potential of targeting  
40    USP7 and RBPJ in anti-tumor immunotherapy strategies.

41    **Keywords:** STS, USP7, RBPJ, UFMylation, ubiquitination, T cell exhaustion, HCC



**Graphical Abstract:** Short-term starvation inhibited CD36 N-glycosylation and down-regulated USP7 UFMylation to prevent RBPJ-maintained T cell exhaustion in liver cancer.

## 48 **Introduction**

49 Short-term starvation (STS) closely relates to immune system balance by regulating chemokine  
50 expression and immune cell activity [1]. It boosts infiltration of beige fat cells and M2 macrophages in  
51 white adipose tissue [1], controls immune cell circulation and colonization [2, 3], and activates  
52 AMPK/PPAR $\alpha$  signaling to raise CCL2 levels, inhibiting monocyte movement from bone marrow to  
53 the periphery [2]. Additionally, fasting increases CXCR4 expression on monocytes through  
54 corticosterone release, prompting their migration back to the bone marrow [3]. Insufficient energy  
55 affects immune response via autophagy, with fasting-induced autophagy supplying antigens to MHC  
56 Class II molecules, crucial for dendritic cells to activate T cells [4]. However, the role of STS in T cell  
57 exhaustion and anti-tumor responses is unclear.

58 UFMylation, a new ubiquitin-like modification, involves a three-enzyme process: activation enzyme  
59 E1 (UBA5), binding enzyme E2 (UFC1), and ligase E3 (UFL1) [5]. However, its modified substrate  
60 spectrum, the regulatory mechanism and the biological process are still unclear, and only a few  
61 substrates have been identified [5]. While UFMylation is known to regulate embryonic development  
62 [6], endoplasmic reticulum homeostasis [7], DNA damage response [8], and interferon response [9], its  
63 impact on immune cells in the tumor microenvironment (TME) is not well understood. Given the  
64 importance of T cells in tumor control and immunotherapy, further investigation into UFMylation's  
65 role in T-cell-mediated anti-tumor immunity is warranted.

66 In this study, we found that STS decreased USP7 UFMylation by blocking CD36 N-glycosylation,  
67 hindering CD36 membrane localization, increasing AMPK phosphorylation, thus reducing USP7  
68 UFMylation. Reduced levels of this modification promoted USP7 ubiquitination and decreased its  
69 stability. As a deubiquitinase, USP7 inhibited RBPJ ubiquitination, enhancing its expression. RBPJ  
70 then bound to the promoters of exhaustion gene *Irf4* [10] or *Tnfrsf1b* [11], leading to T cell exhaustion.  
71 Therefore, STS connected glucose metabolism and T cell exhaustion via three protein post-translational

72 modifications (PTMs), highlighting its significant role in the regulation of T cell-mediated  
73 immunotherapy.

## 74 **Methods**

### 75 **Study design**

76 Details regarding the number of biological replicates, the statistical methods employed, and the *P*  
77 values were provided in the figure legends. Sample sizes were not predetermined using statistical  
78 methods; instead, they were estimated based on preliminary experiments. All in vitro cellular  
79 functional experiments were conducted a minimum of three times, with no exclusion from outliers or  
80 other data points from our analyses. Animal experiments were conducted at least five times, with mice  
81 being randomly assigned to treatment groups by cage. Investigators were blinded to group assignments  
82 during the experiments and outcome assessments. Given the post hoc nature of the study, the analyses  
83 presented should be considered exploratory.

### 84 **T cell treatment strategies**

85 Various mouse HCC models were constructed (**Mouse model**). Following the sacrifice of mice,  
86 primary HCC tissues were dissociated into single cell suspensions (**Isolation of tumor tissue**).  
87 Subsequently, live T cells were isolated through flow cytometry sorting (**Flow cytometry analysis or**  
88 **sorting**). Cell transfection, immunoblotting, immunoprecipitation and RT-qPCR were then employed.

### 89 **Construction**

90 The target genes were PCR-amplified from cDNA, cloned into the pDNA3.1 vector (V79020,  
91 Addgene, MA, USA), and tagged with 6×His, HA, or Myc at the C-terminus.

### 92 **Cell lines**

93 HEK293T (300189, Cytion, Germany) and Hep-53.4 (400200, Cytion) cells were grown in DMEM  
94 (10569010, Gibco, NY, USA) with 10% FBS (10099158, Gibco) and 1% Pen-Strep (HY-K1006,

95 MedChemExpress, NJ, USA), while mouse primary T cells were cultured in T Cell Expansion SFM  
96 (A1048501, Gibco) with the same supplements. To ensure the proliferation of T cells, Dynabeads  
97 Mouse T-Activator CD3/CD28 (11456D, Gibco) was used to activate them. T cells were cultured in  
98 RPMI 1640 medium (11879020, Gibco) with the same supplements for glucose starvation. All cultures  
99 were maintained at 37°C with 5% CO<sub>2</sub>. T cells were treated with A-769662 (3 μM, HY-50662,  
100 MedChemExpress), Cycloheximide (500 nM, HY-12320, MedChemExpress), Dorsomophine (10 μM,  
101 S7840, Selleck, TX, USA), MG132 (40 μM, HY-13259, MedChemExpress), PNGase F (500U, HY-  
102 P2929, MedChemExpress), Swainsonine (40 μM, HY-N6722, MedChemExpress), and Tunicamycin (2  
103 μg/mL, HY-A0098, MedChemExpress) for 48 h, respectively.

#### 104 **Mouse model**

105 All animal experiments followed protocols approved by Fujian Medical University's Ethics Committee  
106 (IACUC FJMU 2023-Y-0841). Mice were kept in ventilated cages in a pathogen-free environment at  
107 room temperature (RT) and 50%-60% humidity. Six mice were randomly assigned per group. Specific  
108 operation strategy:

109 **1)** Construction of subcutaneous tumor model: Hep-53.4 cells ( $5 \times 10^6$ ) were suspended in 100 μL  
110 DPBS (14190144, Gibco) and injected subcutaneously into 10-week-old female C57BL/6J mice (~20  
111 g, GemPharmatech, China). Tumor formation was observed when the control group's average tumor  
112 diameter reached at least 2 mm. When a mouse's tumor reached 2 cm in diameter, it was euthanized  
113 with CO<sub>2</sub>, and the tumor was removed, photographed, and weighed. Tumor volume was calculated  
114 using the formula: (long axis  $\times$  wide axis<sup>2</sup>)  $\times$  0.5.

115 **2)** Construction of primary HCC model: Briefly, a single dose of DEN (25 mg/kg, HY-N7434,  
116 MedChemExpress) was injected into 15-day-old female C57BL/6J mice intraperitoneally (*i.p.*) to  
117 initiate tumor formation. At 4 weeks of age, CCl<sub>4</sub> (0.5 mL/kg, HY-Y0298, MedChemExpress) was  
118 injected *i. p.* Twice a week with CCl<sub>4</sub> for an additional 12 weeks. When HCC was formed in the liver,

119 and confirmation was obtained by bimanual palpation and dissection. Anesthesia and euthanasia during  
120 the experiment: If an animal becomes listless and loses its appetite, it should be euthanized with CO<sub>2</sub>.

121 **3) Construction of patient-derived orthotopic xenograft (PDOX) model:** The study involving patients  
122 was approved by the Ethics Committee of Fujian Medical University Union Hospital (approval number  
123 [2023]173) and performed in accordance with the Helsinki Declaration and government policies.

124 Briefly, mechanically minced pieces of fresh patient HCC tissue were plated on bottles at 37°C in  
125 Human Liver Organoid Culture Medium (abs9529, Absin, China) for up to 2 weeks. Organoids with a  
126 diameter of 300 µm were made with sterile DPBS at a concentration of  $2 \times 10^7$ /mL,  $1 \times 10^6$  cells per  
127 mouse, and an injection volume of 50 µL. huHSC-NCG mice (GemPharmatech) were anesthetized  
128 with 0.8% Pentobarbital Sodium (60 mg/kg, P3761, Merck, Germany) by *i. p.* After anesthesia, the  
129 mice were fixed on the operating board, and the surgical site was disinfected. A longitudinal incision  
130 was made about 1 cm below the xiphoid process of mice to open the abdominal cavity, and the left lobe  
131 of the liver was gently exposed with a sterile cotton swab. Fix the liver lobe with a cotton swab, insert a  
132 1 mL micro-syringe along the liver surface at 15-30°, penetrate the liver of about 0.5 cm, inject the cell  
133 suspension slowly, withdraw the needle slowly, and use a sterile cotton swab to lightly press the  
134 injection site to stop bleeding. The liver was then carefully placed back into the abdominal cavity, the  
135 abdomen was sutured layer by layer, and the incision was sterilized. Place the mice on an electric  
136 blanket until the mice wake up, then return them to their cages and observe the changes in the mice's  
137 vital signs and body weight. Mice (passage 1) were maintained and sacrificed when behavioral  
138 abnormalities (collapse, hyperactivity) and weight loss occurred. Organoids (passage 1) were further  
139 prepared from minced xenograft livers in the same manner as patient tissues and implanted for several  
140 generations. The PDOX model was established at passage 3, when tumor phenotype tended to stabilize.

141 **4) Construction of *Usp7*- or *Rbpj*-conditional knockout (cKO) mice:** To create a *Usp7*-cKO mouse  
142 model (T051806, GemPharmatech), Exon 2-Exon5 of *Usp7*-208 transcript were targeted as the flox  
143 region. For a *Rbpj*-cKO mouse model (NM-CKO-2101541, Shanghai Model Organisms Center,

China), Exon 6-Exon7 were selected. Knocking out these regions would induce the frameshift mutation, leading to premature translation termination and protein mutations. Fertilized eggs were implanted into female C57BL/6J mice to produce positive F0 mice. To achieve T cell-specific deletion, floxed *Usp7* or *Rbpj* mice were bred with *Cd4-Cre* transgenic mice (T004818, GemPharmatech). For animal studies with *Usp7<sup>flox/flox</sup>Cd4-Cre* (*Usp7*-cKO) or *Rbpj<sup>flox/flox</sup>Cd4-Cre* (*Rbpj*-cKO) mice, littermates with *Usp7<sup>flox/flox</sup>* or *Rbpj<sup>flox/flox</sup>* as control were used. Deletion of the floxed *Usp7* allele and wild-type (WT) *Usp7* exons was detected by PCR using the following primers: *Usp7*-5' arm (F- GGTCAAAGAGATTCTGAAGTACCCATT, R-AAACTGGCCCACAATCCCTTG), *Usp7*-3' arm (F- GCACTGGTTTTCCAGTCACAGTG, R-CTTCTTCCCAGCAAACCTTCTGATC). Deletion of the floxed *Rbpj* allele and WT *Rbpj* exons was detected by PCR using the following primers: *Rbpj*-floxed (F-GAAGGTCGGTTGACACCAGATAGC, R-GCAATCCATCTTGTTCATGGCC), *Rbpj*-WT (F- GTTCTTAACCTGTTGGTCGGAACC, R-GCTTGAGGCTTGATGTTCTGTATTGC). Primers that produce T cell-specific KO: 5' arm (F-GGGCAGTCTGGTACTTCCAAGCT, R- AGCATGTCTCAGGGTTCAGCCTAG), WT (F-CAGCAAAACCTGGCTGTGGATC, R- ATGAGCCACCATGTGGGTGTC).

**5) Construction of *Usp7*- or *Rbpj*-conditional knock-in (cKI) mice.** Using CRISPR/Cas9 technology, a CAG-tdTomato-polyA expression frame was inserted into the *Rosa26* gene locus by homologous recombination. A homologous recombination vector containing a 5' homology arm, a tdTomato expression frame, and a 3' homology arm was constructed by In-Fusion cloning. Cas9 mRNA, gRNA, and donor vector were microinjected into fertilized eggs of female C57BL/6J mice to obtain mice with loxp sites and mate with *Cd4-Cre* transgenic mice. For animal studies with *Usp7<sup>flox/flox</sup>Cd4-Cre* (*Usp7*-cKI) or *Rbpj<sup>flox/flox</sup>Cd4-Cre* (*Rbpj*-cKI) mice, littermates with *Usp7<sup>flox/flox</sup>* or *Rbpj<sup>flox/flox</sup>* as control were used. Primers for *Usp7*- or *Rbpj*-cKI identification: WT primers-used to identify the presence of WT alleles and Cas9 activity (F-CCTCTTCCCTCGTGATCTGC, R-TGGAAAATACTCCGAGGCGG), Insert primers-used to identify whether the Donor inserted into the *Rosa26* locus (F-



169 GGGCAACGTGCTGGTTATTG, R-AAGGGTTCCGGATCAGCTTG). Identification of genotype  
170 results: Homozygous: Only Insert primers amplification bands were positive. WT: Only the  
171 amplification bands of WT primers were positive. Heterozygote: The amplified bands of both primers  
172 were positive.

173 **6)** Ark313-*Tnfrsf1b/Irf4*-overexpression (OE) production and tail vein infusion: Ark313 is a  
174 synthetic AAV-6 that exhibits high transduction efficiency in T cells [12]. HEK293T cells were co-  
175 transfected with 11 µg AAV-6 Packaging System (VPK-406, Cell Biolabs, CA, USA), 8 µg AAV-6  
176 Rep-Cap Plasmid (VPK-426, Cell Biolabs), and 6 µg Ark313 [12]-*Tnfrsf1b/Irf4*-OE plasmid using the  
177 AAV-MAX System (A51217, Gibco) for 72 h. Transfected cells were collected in Viral Production  
178 Medium (A4817901, Gibco), lysed by three cycles of rapid freeze/thaw, and then incubated with 25  
179 IU/mL Benzonase (E1014, Merck) for 1 h at 37°C. The high-pressure injection via tail vein was  
180 performed. Briefly, mice were injected with 2 mL of saline containing Ark313-*Tnfrsf1b/Irf4*-OE (5 µg)  
181 within 7 s via the tail vein.

182 **7)** Drug treatment: The drug injection protocol involved administering Abatacept-anti-CTLA4  
183 antibody (10 mg/kg, HY-108829, MedChemExpress), anti-mouse CD3ε antibody (15 mg/kg, A2104,  
184 Selleck), anti-mouse IgG antibody (15 mg/kg, A2150, Selleck), Avagacestat (10 mg/kg, HY-50845,  
185 MedChemExpress), Camrelizumab-anti-PD1 antibody (3 mg/kg, HY-P9971, MedChemExpress), MK-  
186 0752 (100 mg/kg, HY-10974, MedChemExpress), and SB-747651A (5 mg/kg, HY-114038,  
187 MedChemExpress) into the tail vein 20 days before the mice were sacrificed, and then every three days  
188 for a total of five doses. Equal volume of DMSO (HY-Y0320, MedChemExpress) or normal saline  
189 (IN9012, Solarbio, China) was used as the control group.

190 **8)** STS conditions: Mice underwent complete food deprivation with free access to water for two  
191 cycles of 48 h and one cycle of 24 h [13].

## 192 **Cell Cycle Detection**

193 T cells ( $1 \times 10^5$ ) were fixed overnight with 70% ethanol (100983, Merck). The cells were resuspended  
194 in 250  $\mu$ L of FxCycle™ PI/RNase Staining Solution (F10797, Invitrogen, CA, USA), mixed, and  
195 incubated for 20 min at 4°C. Relative light units were detected by BD FACSAria™ III Cell Sorter (BD  
196 Biosciences, NJ, USA) within 1 h.

## 197 **Cell transfection**

198 For electrotransfection: T cells were suspended in Opti-MEM™ I Reduced Serum Medium (31985062,  
199 Gibco) at a concentration of  $10^7$  cells/mL. Plasmid DNAs were added into the suspension to achieve a  
200 final concentration of 10 mg/mL. The pulses were generated by using a Nxt Electroporation System  
201 (NEON18SK, Thermo Scientific, CA, USA). After electrotransfection, samples were incubated at 37°C  
202 for 10 min to promote endocytosis. For gene KO, mouse CRISPR target sequence was designed and  
203 synthesized: *Ampk* (GAAGATTCTGGAGCCTTGACG), *Cd36* (TGTGCAAAACCCAGATGACG),  
204 *Hmgcr* (TCATCATCCTGACGATAACG), *Insr* (TTGTTCCGGATGTCCATACC), *Pdli*  
205 (TCCAAAGGACTTGTACGTGG), *Ufl1* (AGAGACGAGCTACATGTCCG), *Ufsp2*  
206 (GGGTCGATATCTCCAGCATG), and *Usp7* (GCGCTCGACAGTGAAGTAA).

## 207 **CUT&Tag assay**

208 We conducted the CUT&Tag assay using CUT&Tag Assay Kit (77552, Cell Signaling Technology,  
209 MA, USA). 100,000 cells were lysed, and the lysate was treated with Con A-coated magnetic beads for  
210 1 h at RT. This was followed by a 2-h incubation with anti-RBPJ antibody (720219, Invitrogen), a 1-h  
211 incubation with a secondary antibody (31460, Invitrogen), and a 1-h incubation with a pA/G-Tn5 linker  
212 complex. Indexed libraries were pooled based on cell count and sequenced on a NovaSeq 6000  
213 (Illumina, CA, USA) with paired-end 150 bp.

214 For CUT&Tag data analysis, Fastp [14] was used to trim adaptors and remove low-quality reads,  
215 producing high-quality clean reads that were aligned to the mm39 genome. Deeptools [15] calculated  
216 and plotted correlation and read distribution heatmaps. MACS3 [16] identified peaks, excluding

217 blacklist regions. ChIPSeeker [17] annotated peaks, and Homer identified motifs. MANorm2 [18]  
218 detected differentially enriched regions between sample groups. ClusterProfiler conducted GO and  
219 KEGG enrichment analyses on genes linked to the differentially enriched regions. Enriched peaks were  
220 visualized using IGV [19]. NewCore BioTechnology (Shanghai, China) provided bioinformatics  
221 support.

## 222 **Cytometry by time-of-flight (CyTOF)**

223 Antibody labeling: Antibodies were conjugated to isotopically enriched lanthanide metals using the  
224 Maxpar X8 Antibody Labeling Kit (NC1648790, Standard BioTools, CA, USA). The labeled  
225 antibodies were stored in DPBS supplemented with 1% glycerol (1295731, Merck), 0.05% BSA  
226 (AM2616, Invitrogen), and 0.05% sodium azide (S2002, Merck) at 4°C. Antibody used in this study:  
227 anti-BTLA (PA5-95592, Invitrogen), anti-CD3E (14-0032-82, Invitrogen), anti-CD4 (14-0041-82,  
228 Invitrogen), anti-CD8A (14-0808-82, Invitrogen), anti-CD25 (14-0251-86, Invitrogen), anti-CD27 (14-  
229 0271-82, Invitrogen), anti-CD39 (14-0391-82, Invitrogen), anti-CD44 (14-0441-82, Invitrogen), anti-  
230 CD45 (14-0451-82, Invitrogen), anti-CD62L (MA1-10262, Invitrogen), anti-CD69 (MA1-207,  
231 Invitrogen), anti-CD80 (14-0801-82, Invitrogen), anti-CD95 (14-0951-85, Invitrogen), anti-CD127  
232 (14-1271-82, Invitrogen), anti-CD152 (14-1522-82, Invitrogen), anti-CD160 (14-1601-81, Invitrogen),  
233 anti-CD223 (14-2231-82, Invitrogen), anti-CD279 (11-9985-82, Invitrogen), anti-GZMB (PA5-13518,  
234 Invitrogen), anti-IFNG (MM700, Invitrogen), anti-IL2 (14-7021-81, Invitrogen), anti-IL6 (M620,  
235 Invitrogen), anti-IL21 (PA5-46962, Invitrogen), anti-KI67 (MA5-14520, Invitrogen), anti-KLRG1  
236 (ab25054, Abcam, UK), anti-Perforin (ab261727, Abcam), anti-TBX21 (PA5-109245, Invitrogen),  
237 anti-TCF7 (MA5-14965, Invitrogen), anti-TCR $\beta$  (14-5961-82, Invitrogen), anti-TCR $\gamma\delta$  (14-5711-82,  
238 Invitrogen), anti-TIGIT (MA5-48199, Invitrogen), anti-TNFA (PA1-40281, Invitrogen), anti-TOX  
239 (A700-212, Invitrogen), anti-VISTA (MA5-48237, Invitrogen), and anti-2B4 (14-2441-82, Invitrogen)  
240 antibodies.

241 Cell staining: Collect single cell suspension, add 1  $\mu$ L of Cisplatin (201064, Standard BioTools) with  
242 a final concentration of 5  $\mu$ M to distinguish live cells from dead cells, incubate at 37°C for 5 min, and  
243 then add five times the volume of Cell Staining Buffer (201068, Standard BioTools) to terminate the  
244 labeling reaction. Centrifuge at  $300 \times g$  for 5 min, discard the supernatant, and resuspend the cells in  
245 Cell Staining Buffer. To detect cytokine expression, stimulate the cells with Cell Stimulation Cocktail  
246 (plus protein transport inhibitors) (00-4975-93, eBioscience, CA, USA) for 6 h. After stimulation, the  
247 cells were centrifuged at  $300 \times g$  for 5 min and diluted to 1 mL with Cell Staining Buffer to terminate  
248 the stimulation. Nonspecific signals were blocked by adding 5  $\mu$ L Fc Receptor Binding Inhibitor  
249 Polyclonal Antibody (14-9161-73, eBioscience), followed by staining with pre-mixed surface  
250 antibodies at 4°C for 30 min. After washing the cells twice with Cell Staining Buffer, the cells were  
251 fixed in 200  $\mu$ L of Fix and Perm Buffer (201067, Standard BioTools) containing 250 nM Intercalator-Ir  
252 (201192A, Standard BioTools) at 4°C overnight. The cells were washed twice with Cell Staining  
253 Buffer and stained with premixed intracellular antibodies at 4°C for 30 min. The cells were washed  
254 twice with Nuclear Antigen Staining Buffer (201063, Standard BioTools), resuspended in Cell  
255 Acquisition Solution Plus for CyTOF XT (201244, Standard BioTools), and then mixed with 20% EQ  
256 Four Element Calibration Beads (201078, Standard BioTools). Data were acquired using a CyTOF XT  
257 (Standard BioTools) and saved as fcs files.

258 Preprocessing of mass cytometry data: Raw data were normalized using the MATLAB version of the  
259 Normalizer tool [20]. Cells were assigned by manually gating on Event length and DNA ( $^{191}\text{Ir}$  and  
260  $^{193}\text{Ir}$ ) channels, followed by the dead cell discrimination analyzing  $^{195}\text{Pt}$  expression using a FlowJo (BD  
261 Biosciences). Doublets were excluded using Gaussian discrimination channels. Next, data were  
262 concatenated and de-barcoded using Boolean gating. The normalized data containing living cells from  
263 every individual sample were manually exported from FlowJo and imported into R using the  
264 “flowCore” [21] and “flowWorkspaceData” [22]. Before automated high-dimensional data analysis, the  
265 mass cytometry data were transformed with a cofactor in the range of 5 and 60 using an inverse

266 hyperbolic sine function [23]. Living, single cells were exported and imported into R. Before  
267 automated high-dimensional data analysis, data were transformed using an inverse hyperbolic sine  
268 function with a cofactor in the range of between 300 and 600. Additionally, all data were normalized  
269 between 0 and 1 to match the 99-999<sup>th</sup> percentile of the combined samples in each batch.

270 Automated subset identification: To identify T cell subsets accurately, we first performed step 1 of  
271 FlowSOM clustering on the preprocessed and combined mass cytometry dataset to generate a starting  
272 point of 100 nodes [24]. The respective k-value was manually chosen (in the range of between 20 and  
273 30); identified subsets were annotated and merged based on a similarity of antigen expression to uphold  
274 the biological relevance of the dataset. Manually annotated subsets were used to calculate the relative  
275 frequencies of T cell subsets. Heatmaps showed the median expression levels of all markers for each  
276 merged subset and were plotted using the “pheatmap”. From mass cytometry datasets, we pre-selected  
277 major subsets and performed additional FlowSOM [24] analysis to identify smaller cell subsets. We  
278 calculated the median antigen expression among selected cell types of the mass cytometry batch using  
279 the “dplyr”. For data visualization, we applied dimensionality reduction techniques. For a complex  
280 overview of the immune compartment, we used t-SNE [25]. To create a t-SNE of isolated T cells, we  
281 pooled equally proportioned 120,000 T cells from the datasets from the CyTOF batch.

## 282 **Detection of histone H3 modification**

283 Histone H3 modification levels were detected using EpiQuik Histone H3 Modification Multiplex Assay  
284 Kit (P-3100-96, Epigentek, NY, USA). Add 40 ul of sample or standard to the well and incubate at  
285 37°C for 30 min. Wash three times with DPBS, add 50 ul of enzyme-labeled antibody, incubate at RT  
286 for 30 min, add 50 ul of chromogenic solution and 50 ul of stop solution. The absorbance value of each  
287 sample at a wavelength of 450 nm was measured with Multiskan™ FC System (Thermo Fisher).

## 288 **DNA pull-down assay**

289 500 µg of nuclear protein extract, 5 µg of biotin-labeled promoter double-stranded oligonucleotide  
290 probe, and 100 µL of streptavidin magnetic beads (Bes5004, Bersinbio, China) were incubated  
291 overnight at 4°C. After centrifugation at 5000 × g for 5 min in a precooled fixed-angle centrifuge, the  
292 protein-DNA-probe complex was resuspended in 30 µL of loading buffer, and the mixture was boiled  
293 for 10 min. The complexes were separated using immunoblotting.

#### 294 **Flow cytometry analysis or sorting**

295 The cells were resuspended in Flow Cytometry Staining Buffer (00-4222-57, eBioscience), stained  
296 with fluorescent dye-conjugated antibodies for 30 min, and washed twice. Samples were collected  
297 using the BD FACS Aria™ III Cell Sorter and analyzed with FlowJo. During cell sorting, the  
298 concentration was maintained at  $1 \times 10^7$  cells/mL, with a pressure of 60 psi, a 70 µm nozzle, and a  
299 maximum rate of 20,000 events/s. Antibodies used in this study: anti-human-CD3E-BV786 (740961,  
300 BD Biosciences), anti-human-CD4-FITC (550628, BD Biosciences), anti-human-CD8A-V450  
301 (561426, BD Biosciences), anti-human-CD45-BV510 (563204, BD Biosciences), anti-human-PD1-  
302 APC (558694, BD Biosciences), anti-human-TIGIT-PerCP-Cy5.5 (46-9501-82, Invitrogen), anti-  
303 human/mouse-TOX (A700-212, Invitrogen), anti-mouse-CD3E-BV786 (417-0031-82, Invitrogen),  
304 anti-mouse-CD4-FITC (11-0041-82, Invitrogen), anti-mouse-CD8A-APC (17-0081-82, Invitrogen),  
305 anti-mouse-CD36 (MA5-14112, Invitrogen), anti-mouse-CD45-AF700 (56-0451-82, Invitrogen), anti-  
306 mouse-CD45-BV510 (567800, BD Biosciences), anti-mouse-CTLA4 (106311, Biolegend, CA, USA),  
307 anti-mouse-CTLA4-FITC (HMCD15201, Invitrogen), anti-mouse-PD1-BV421 (404-9981-82,  
308 Invitrogen), anti-mouse-PD1-PE (12-9985-82, Invitrogen), anti-mouse-PD1-V450 (75-9981, Cytex,  
309 CA, USA), anti-mouse-TIM3-PerCP-Cy5.5 (134011, Biolegend) antibodies. Viability dye used in this  
310 study: Fixable Viability Stain 575V (565694, BD Biosciences), and Fixable Viability Stain 780  
311 (565388, BD Biosciences).

#### 312 **Immunoblotting and immunoprecipitation**

313 The cells were washed with DPBS, lysed using Novex Tricine SDS Sample Buffer (LC1676,  
314 Invitrogen) with 1% PMSF (36978, Thermo Scientific), boiled for 20 min, and analyzed by sodium  
315 dodecyl sulfate–polyacrylamide gel electrophoresis. For immunoprecipitation, lysate was incubated  
316 with primary antibodies for 1 h at 4°C, then with Protein A/G Magnetic Beads (88802, Thermo  
317 Scientific) for 2 h at 4°C. The complexes were washed and subjected to electrophoresis. Antibodies  
318 used in this study: anti-AMPK (MA5-15815, Invitrogen), anti-CD36 (MA5-14112, Invitrogen), anti-  
319 Flag Tag (MA1-91878, Invitrogen), anti-GFP (MA5-15256, Invitrogen), anti-HA Tag (26183,  
320 Invitrogen), anti-Histone H3 (PA5-16183, Invitrogen), anti-HMGCR (PA5-37367, Invitrogen), anti-  
321 H3S10P (PA5-17869, Invitrogen), anti-INSR (MA5-13783, Invitrogen), anti-IRF4 (14-9858-82,  
322 Invitrogen), anti-Myc Tag (PA1-981, Invitrogen), anti-PD1 (14-9969-82, Invitrogen), anti-pAMPK-  
323 Ser485 (PA5-117221, Invitrogen), anti-RBPJ (720219, Invitrogen), anti-TNFRSF1B (MA5-32618,  
324 Invitrogen), anti-UFL1 (A303-456A, Invitrogen), anti-UFM1 (PA5-90754, Invitrogen), anti-UFSP2  
325 (PA5-99002, Invitrogen), anti-USP7 (PA5-34911, Invitrogen), anti- $\beta$ -actin (MA1-140, Invitrogen), and  
326 anti-6 $\times$ -His Tag (MA1-21315, Invitrogen) antibodies.

### 327 **Immunofluorescence**

328 Cells were fixed with Fixative Solutions (I28800, Thermo Scientific) and blocked with 5% BSA for 1 h  
329 and incubated with anti-H3S10P antibody (PA5-17869, Invitrogen) overnight at 4°C. After three  
330 washes with DPBS, cells were incubated with Goat Anti-Rabbit IgG H&L-AF647 antibody (ab150079,  
331 Abcam). Photographs were taken with the Vectra3 Automated Quantitative Pathology Imaging system  
332 (Akoya Biosciences, MA, USA).

### 333 **Isolation of tumor tissue**

334 The primary HCC tissue was diced into 1-3 mm pieces and digested with Tissue Digestion Solution  
335 (41423ES10, Yeasen, China) at 37°C for 30 min. EDTA (10 mM, HY-Y0682, MedChemExpress) was  
336 added to stop the reaction. The sample was homogenized using a 23 G needle, strained through a 70

337 mm filter, and centrifuged at  $400 \times g$  for 8 min. Then, it was centrifuged at  $900 \times g$  for 30 min in 30%  
338 Percoll (40501ES60, Yeasen) to isolate the middle white cell layer. The cells were washed twice with  
339 DPBS for flow cell sorting.

#### 340 **Liquid chromatography-mass spectrometry (LC-MS)**

341 Proteins were extracted by 8 M urea (U4883, Merck) with 1% PMSF. Then, the proteins were  
342 subjected to Trypsin (HY-129047, MedChemExpress) digestion at an enzyme/protein mass ratio of  
343 1:50 overnight following the Filter-Aided Sample Preparation procedure [26]. Specifically, the proteins  
344 were subjected to reductive alkylation with Dithiothreitol (D0632, Merck) for 30 min at  $56^{\circ}\text{C}$  and  
345 Iodoacetamide (A3221, Merck) for 30 min at RT. Then, the samples were loaded into 10 kDa  
346 Centrifugal Filter Unit with Ultracel (MRCPRT010, Millipore), and the urea was diluted and replaced  
347 by  $\text{NH}_4\text{HCO}_3$  (5438350100, Merck) gradually after centrifugation for twice with 50 mM  $\text{NH}_4\text{HCO}_3$ .  
348 Proteins were digested with Trypsin overnight at  $37^{\circ}\text{C}$ . Finally, purified peptide was acquired after  
349 extraction with 50% Acetonitrile (34851, Merck) and 0.1% Formic acid (06473, Merck). The peptides  
350 were dried in a vacuum at  $60^{\circ}\text{C}$  before LC-MS analysis.

#### 351 **LC-MS analysis**

352 The peptides were subjected to LC-MS analysis using an Orbitrap Fusion Lumos Tribrid Mass  
353 Spectrometer (Thermo Scientific) coupled with an EASY-nLC™ 1000 (Thermo Scientific). Dried  
354 peptide was re-suspended in loading buffer and loaded onto a 100 C18 HPLC Columns ( $100 \mu\text{m} \times 2$   
355 cm, homemade; particle size,  $3 \mu\text{m}$ ; pore size,  $120\text{\AA}$ , Thermo Scientific) with a maximum pressure of  
356 280 bar using solution A. Then, the peptides were separated on a 100 C18 HPLC Columns ( $150 \mu\text{m} \times$   
357 12 cm, homemade; particle size,  $1.9 \mu\text{m}$ ; pore size,  $120\text{\AA}$ ) with a gradient of 5 ~ 35% mobile phase B,  
358 and adjusted as a series of linear gradients following the different hydrophilic properties of six  
359 fractions, respectively, at a flow rate of 600 nl/min for 75 min. The MS analysis was performed by  
360 scanning m/z values from 300 to 1400 and a resolution of 120,000 at 200 m/z. An automatic gain



361 control target value of  $5 \times 10^5$  was used, with a maximum injection time of 50 ms for full scans. The  
362 top-speed mode was selected with a 1.6 m/z window and fragmented by higher energy collisional  
363 dissociation at a normalized collision energy of 35%. Then measurements were taken using ion trap  
364 analyzer with an automatic gain control target of  $5 \times 10^3$  and a maximum injection time of 35 ms for  
365 MS/MS scans. Finally, the dynamic exclusion time was set at 18 s, and data were acquired by Xcalibur  
366 2.2 (Thermo Scientific).

### 367 **Peptide and protein identification**

368 MS raw files were processed with the “Firmiana” [27] against the mouse RefSeq protein database. The  
369 maximum number of missed cleavages was set to 2. Mass tolerances of 20 ppm for precursor and 0.5  
370 Da for production were allowed. For quality control of protein identification, the target-decoy-based  
371 strategy was applied to confirm that the false discovery rate (FDR) of both peptide and protein was  
372 lower than 1%. The program percolator was used to obtain probability value ( $q$  value) and showed that  
373 the FDR of every peptide-spectrum match was lower than 1%. Then all peptides shorter than seven  
374 amino acids were removed. The cut-off ion score for peptide identification was 20. All the peptide-  
375 spectrum matches in all fractions were combined for protein quality control, which was a stringent  
376 quality control strategy. The  $q$  values of both target and decoy peptide sequences were dynamically  
377 increased until the corresponding protein FDR was less than 1% employing the parsimony principle.  
378 Finally, to reduce the false positive rate, the proteins with at least one unique peptide were selected for  
379 further investigation.

### 380 **Label-free-based MS quantification of proteins**

381 “Firmiana” [27] was employed for protein quantification. Here, the identification results and the raw  
382 data from mzXML file were loaded into the “Firmiana”. Then for each identified peptide, the XIC  
383 (extracted-ion chromatogram) was extracted by searching against the MS1 based on its identification  
384 information, and the abundance was estimated by calculating the area under the extracted XIC curve.

385 For protein abundance calculation, the nonredundant peptide list was used to assemble proteins  
386 following the parsimony principle. Then, the protein abundances were firstly corrected by deploying a  
387 traditional label-free, iBAQ algorithm, which used number of theoretical peptides to correct the  
388 differences in signal intensity caused by protein size and sequence.

### 389 **Mass spectrometry (MS)**

390 Protein bound to USP7 was isolated with anti-USP7 antibody (PA5-34911, Invitrogen) and sent to 10K  
391 Genomics (Shanghai, China) for analysis.

### 392 **Molecular docking analysis of protein with protein**

393 HDOCK [12] was used as a molecular docking program to analyze the interaction among proteins.  
394 PyMol was used to separate the original ligand and protein structure, dehydrate to remove organic  
395 matter, and then the Prepare module of Discovery Studio was used to prepare the protein, such as  
396 hydrogenation and protonation. LigPlus [28] was performed to analyze the forces between two proteins  
397 in two dimensions. The protein interaction interface was analyzed using the Analysis Interface module  
398 of Discovery Studio, and PyMol was applied to draw the interacting amino acid residues between two  
399 proteins.

### 400 **RT-qPCR**

401 Total RNA was extracted using the FastPure Cell/Tissue Total RNA Isolation Kit V2 (RC112-01,  
402 Vazyme, China), then reverse transcribed with HiScript II Q Select RT SuperMix (R233-01, Vazyme).  
403 RT-qPCR was conducted on Applied Biosystems systems with ChamQ SYBR qPCR Master Mix  
404 (Q311-02, Vazyme). The PCR cycle was 95°C for 30s, then 40 cycles of 95°C for 10s, 63°C for 10s,  
405 and 72°C for 30s. Gene expression was analyzed using the  $2^{-\Delta\Delta CT}$  method. Primers for mRNA: *Irf4* (F-  
406 TCCGACAGTGGTTGATCGAC, R-CCTCACGATTGTAGTCCTGCTT), *Rbpj* (F-  
407 ATGCCCTCCGGTTTTCTC, R-GGACAAGCCCTCCGAGTAGT), *Tnfrsf1b* (F-  
408 ACACCCTACAAACCGGAACC, R-AGCCTTCCTGTCATAGTATTCCT), *Usp7* (F-

409 AAGTCTCAAGGTTATAGGGACGG, R-CCATGCTTGTCTGGGTATAGTGT), and  $\beta$ -actin (F-  
410 GGCTGTATTCCCCTCCATCG, R-CCAGTTGGTAACAATGCCATGT).

### 411 **Transcriptome Sequencing**

412 Total RNA was extracted and purified with FastPure Cell/Tissue Total RNA Isolation Kit V2. RNA-  
413 seq libraries were constructed with VAHTS® mRNA-seq V3 Library Prep Kit for Illumina (NR611,  
414 Vazyme). Sequencing was performed using Illumina NovaSeq 6000 platform (provided by 10K  
415 Genomics), and the sequencing depth of each sample was 6G bases.

### 416 **Statistical analysis**

417 We used SPSS 19.0 (IBM, NY, USA) and R 4.4 (Lucent Technologies, NJ, USA) software for  
418 statistical analysis, and Prism 9.0 (GraphPad, CA, USA) and R 4.4 software to generate visual images.  
419 All data were expressed as mean  $\pm$  SD and reported *P* values less than 0.05 were considered  
420 statistically significant. Normality analyses were conducted using Shapiro-Wilk test and D'Agostino  
421 and Pearson tests. When comparing two samples, the independent sample *t* test was used if the data  
422 were normally distributed, and the variances were homogeneous. Otherwise, Wilcoxon rank sum test  
423 was used. Kaplan-Meier curves with 95% confidence intervals were plotted and the Log-rank test was  
424 used to compare survival curves.

## 425 **Results**

### 426 **STS alleviated T cell exhaustion in HCC**

427 Recent findings indicated that STS boosts T cell-based immunotherapy [29, 30]. We examined STS's  
428 effects on T cells infiltrating HCC and found that STS, compared to a standard diet, reduced tumor  
429 growth (Figure 1A-1D), improved prognosis (Figure 1E), increased T cell infiltration (Figure 1F, S1A),  
430 and decreased PD1 expression in CD3<sup>+</sup> T cells (Figure 1F). Our study demonstrated that the  
431 neutralization of T cells attenuated the tumor-inhibitory effects of STS, suggesting that STS facilitated  
432 tumor suppression primarily through the enhancement of T cell function and infiltration (Figure 1G-

1K). Furthermore, STS exhibited anticancer properties in tumor-bearing subjects with T cell deficiency (Figure 1G-1K). We hypothesized that this effect may be attributed to the impediment of tumor cell proliferation due to caloric restriction [31]. Using mass cytometry, we detailed STS's effects on infiltrating T cells, finding that STS significantly altered T cell function (Figure 1L). Compared with CD4<sup>+</sup> T cells, CD8<sup>+</sup> T cells were more significantly affected by STS (Figure S1B). It increased CD3<sup>+</sup> T cell infiltration and inhibited four exhaustion genes (LAG3, PD1, TOX, and 2B4) expression in CD4<sup>+</sup> T cells and six exhaustion genes (CD39, CTLA4, PD1, TIGIT, TOX, and VISTA) expression in CD8<sup>+</sup> T cells (Figure S1C, S1D). It also increased the expression of effector IL21 in CD4<sup>+</sup> or CD8<sup>+</sup> T cells and proliferation marker KI67 in CD4<sup>+</sup> T cells (Figure S1C, S1D).

Hierarchical clustering heatmap identified 16 T cell subsets (Figure 1M), including IL7R<sup>+</sup> CD25<sup>+</sup> γδT cells, CD27<sup>+</sup> TCF7<sup>+</sup> CD4<sup>+</sup> T cells, CD27<sup>+</sup> IFNG<sup>+</sup> CD8<sup>+</sup> T cells, PD1<sup>+</sup> TCF7<sup>+</sup> γδT cells, CD39<sup>+</sup> TOX<sup>+</sup> CD8<sup>+</sup> T cells, CD44<sup>+</sup> TCF7<sup>+</sup> CD8<sup>+</sup> T cells, CD69<sup>+</sup> CD44<sup>+</sup> CD8<sup>+</sup> T cells, CD69<sup>+</sup> TCF7<sup>+</sup> CD4<sup>+</sup> T cells, CD69<sup>+</sup> TCF7<sup>+</sup> CD8<sup>+</sup> T cells, CD95<sup>+</sup> TOX<sup>+</sup> CD8<sup>+</sup> T cells, IL2<sup>+</sup> TCF7<sup>+</sup> CD8<sup>+</sup> T cells, KI67<sup>+</sup> TCF7<sup>+</sup> CD4<sup>+</sup> T cells, KI67<sup>+</sup> TCF7<sup>+</sup> CD8<sup>+</sup> T cells, TBET<sup>+</sup> CD69<sup>+</sup> CD8<sup>+</sup> T cells, TBET<sup>+</sup> CD69<sup>+</sup> CD4<sup>+</sup> T cells, and TNFA<sup>+</sup> TCF7<sup>+</sup> CD8<sup>+</sup> T cells (Figure 1N). Post-STS, CD27<sup>+</sup> TCF7<sup>+</sup> CD4<sup>+</sup> T cells, CD44<sup>+</sup> TCF7<sup>+</sup> CD8<sup>+</sup> T cells, CD69<sup>+</sup> TCF7<sup>+</sup> CD4<sup>+</sup> T cells, KI67<sup>+</sup> TCF7<sup>+</sup> CD4<sup>+</sup> T cells, TBET<sup>+</sup> CD69<sup>+</sup> CD8<sup>+</sup> T cells, TBET<sup>+</sup> CD69<sup>+</sup> CD4<sup>+</sup> T cells, CD27<sup>+</sup> IFNG<sup>+</sup> CD8<sup>+</sup> T cells, KI67<sup>+</sup> TCF7<sup>+</sup> CD8<sup>+</sup> T cells, CD69<sup>+</sup> CD44<sup>+</sup> CD8<sup>+</sup> T cells, IL2<sup>+</sup> TCF7<sup>+</sup> CD8<sup>+</sup> T cells, PD1<sup>+</sup> TCF7<sup>+</sup> γδT cells, TNFA<sup>+</sup> TCF7<sup>+</sup> CD8<sup>+</sup> T cells increased, and CD39<sup>+</sup> TOX<sup>+</sup> CD8<sup>+</sup> T cells, CD69<sup>+</sup> TCF7<sup>+</sup> CD8<sup>+</sup> T cells, CD95<sup>+</sup> TOX<sup>+</sup> CD8<sup>+</sup> T cells decreased (Figure 1O, 1P).

Additionally, we investigated the impact of STS-stimulated and STS-pre-stimulated tumor cells on T cell exhaustion in vitro to analyze whether STS directly regulates T cells or indirectly influences T cells through tumor cells. Our findings indicated that both conditions inhibited the expression of inhibitory receptors on T cells (Figure S2A-S2C). We first investigated why STS-pre-stimulated tumor cells suppressed inhibitory receptor expression on T cells. Given that AMPK activation leads to the

458 phosphorylation of PDL1 at Ser283, resulting in its degradation [32], and that an insufficient energy  
459 supply inevitably activates the AMPK pathway [33], we proceeded to knock out *Ampk* and *Pd1l* in  
460 Hep-53.4 cells. Our results demonstrated that *Ampk*-KO tumor cells up-regulated the expression of  
461 PD1 and TIM3 on CD8<sup>+</sup> T cells, which were inhibited by STS, while *Pd1l*-KO tumor cells reduced the  
462 elevated expression of PD1 and TIM3 on CD8<sup>+</sup> T cells induced by *Ampk*-KO (Figure S2C-S2D). These  
463 findings suggested that STS inhibited PDL1 expression by activating AMPK phosphorylation in tumor  
464 cells, thereby protecting T cells from exhaustion. Next, we investigated the molecular mechanisms by  
465 which STS protected T cells from dysfunction from the perspective of T cells themselves.

#### 466 **STS alleviated T cell exhaustion by inhibiting USP7**

467 The oncogenic potential of TME is modulated by the interplay between nutritional deficiencies and  
468 ubiquitin proteasome systems [34]. Nonetheless, the interaction between STS and deubiquitinase in T  
469 cells remains unexplored. We investigated STS's effects on deubiquitinase expression. Mass  
470 spectrometry (MS) and immunoblotting assays revealed that STS exclusively inhibited USP7  
471 expression in CD3<sup>+</sup> T cells (Figure 2A, 2B) without affecting its transcription (Figure 2C). It is  
472 essential to first ascertain whether STS suppressed USP7 expression in tumor cells and to understand  
473 the subsequent impact on the susceptibility of these cells to T cell-mediated cytotoxicity. Previous  
474 research has demonstrated that USP7 plays a protective role in preventing the degradation of PDL1,  
475 thereby reducing the susceptibility of tumor cells to T cell-mediated cytotoxicity [35]. Consequently, it  
476 is imperative to ascertain whether STS inhibit USP7 expression in tumor cells to potentiate T cell  
477 function. Our findings indicated that STS suppressed USP7 expression in Hep-53.4 cells (Figure S3A),  
478 and the KO of *Usp7* in Hep-53.4 cells resulted in inhibited tumor growth (Figure S3B-S3D), with the  
479 inverse also being true (Figure S3E-S3G). Moreover, *Usp7*-KO in Hep-53.4 cells led to reduced PDL1  
480 expression (Figure S3H), and the reverse was observed as well (Figure S3I). Rescue experiments  
481 revealed that STS diminished the expression of both USP7 and PDL1 in Hep-53.4 cells, while *Usp7*-

482 OE mitigated the inhibitory effect of STS on PDL1 expression (Figure S3J). In vivo studies further  
483 demonstrated that STS impeded tumor growth, and this inhibitory effect was attenuated by *Usp7*-OE in  
484 tumor cells (Figure S3K-S3M). Additionally, the tumor-promoting effect of *Usp7*-OE was counteracted  
485 by *Pd1l*-KO (Figure S3N-S3P), suggesting that STS exerted its effects by inhibiting USP7, thereby  
486 reducing PDL1 expression and enhancing the sensitivity of tumor cells to T cell-mediated killing.  
487 Following this, we investigated the role of USP7 in T cells, specifically focusing on its influence on T  
488 cell exhaustion.

489 Our study indicated that overexpressing *Usp7* increased PD1 expression in CD3<sup>+</sup> T cells, whereas  
490 inhibiting it reduced PD1 levels (Figure 2D). In vivo, *Usp7*-cKO suppressed tumor growth (Figure 2E-  
491 2H) and improved prognosis (Figure 2I). Mass cytometry was also used to detail *Usp7*-cKO's  
492 regulatory impact on T cells, and non-metric Multidimensional Scaling (NMDS) analysis indicated that  
493 *Usp7*-cKO significantly changed T cell function (Figure 2J). Hierarchical clustering heatmap identified  
494 15 T cell subsets (Figure 2K), including IL7R<sup>+</sup> CD95<sup>+</sup>  $\gamma\delta$ T cells, GZMB<sup>+</sup> CD25<sup>+</sup>  $\gamma\delta$ T cells, CD39<sup>+</sup>  
495 TOX<sup>+</sup> CD8<sup>+</sup> T cells, CD69<sup>+</sup> TCF7<sup>+</sup> CD4<sup>+</sup> T cells, CD69<sup>+</sup> TCF7<sup>+</sup>  $\gamma\delta$ T cells, CD95<sup>+</sup> TOX<sup>+</sup> CD8<sup>+</sup> T cells,  
496 IL2<sup>+</sup> TCF7<sup>+</sup> CD4<sup>+</sup> T cells, KLRG1<sup>+</sup> CD44<sup>+</sup> CD4<sup>+</sup> T cells, TBET<sup>+</sup> CD69<sup>+</sup> CD8<sup>+</sup> T cells, TBET<sup>+</sup> CD69<sup>+</sup>  
497 CD4<sup>+</sup> T cells, TCF7<sup>+</sup> CD69<sup>+</sup> CD8<sup>+</sup> T cells, TCF7<sup>+</sup> CD69<sup>+</sup>  $\gamma\delta$ T cells, TCF7<sup>+</sup> KI67<sup>+</sup> CD4<sup>+</sup> T cells,  
498 TNFA<sup>+</sup> TCF7<sup>+</sup> CD8<sup>+</sup> T cells, and IFNG<sup>+</sup> CD27<sup>+</sup> CD8<sup>+</sup> T cells (Figure 2L). Post-*Usp7* loss, CD69<sup>+</sup>  
499 TCF7<sup>+</sup> CD4<sup>+</sup> T cells, IL2<sup>+</sup> TCF7<sup>+</sup> CD4<sup>+</sup> T cells, KLRG1<sup>+</sup> CD44<sup>+</sup> CD4<sup>+</sup> T cells, TBET<sup>+</sup> CD69<sup>+</sup> CD8<sup>+</sup> T  
500 cells, TBET<sup>+</sup> CD69<sup>+</sup> CD4<sup>+</sup> T cells, TCF7<sup>+</sup> CD69<sup>+</sup> CD8<sup>+</sup> T cells, TCF7<sup>+</sup> KI67<sup>+</sup> CD4<sup>+</sup> T cells, IFNG<sup>+</sup>  
501 CD27<sup>+</sup> CD8<sup>+</sup> T cells, TCF7<sup>+</sup> CD69<sup>+</sup>  $\gamma\delta$ T cells, GZMB<sup>+</sup> CD25<sup>+</sup>  $\gamma\delta$ T cells, TNFA<sup>+</sup> TCF7<sup>+</sup> CD8<sup>+</sup> T cells  
502 increased, while CD39<sup>+</sup> TOX<sup>+</sup> CD8<sup>+</sup> T cells, CD69<sup>+</sup> TCF7<sup>+</sup>  $\gamma\delta$ T cells, CD95<sup>+</sup> TOX<sup>+</sup> CD8<sup>+</sup> T cells,  
503 IL7R<sup>+</sup> CD95<sup>+</sup>  $\gamma\delta$ T cells decreased (Figure 2M, 2N). In addition, it increased CD3<sup>+</sup> T cell infiltration  
504 and inhibited three exhaustion genes (CD39, CD95, and TOX) expression in CD4<sup>+</sup> T cells and five  
505 exhaustion genes (CTLA4, PD1, TIGIT, TOX, and VISTA) expression in CD8<sup>+</sup> T cells (Figure 2O,  
506 S3Q). It also increased the expression of IL21 in CD4<sup>+</sup> or CD8<sup>+</sup> T cells and KI67 in CD4<sup>+</sup> T cells

507 (Figure 2O, S3Q). Furthermore, we used mice *Usp7*-cKI to analyze if STS's anticancer effects rely on  
508 USP7 inhibition. As expected, *Usp7*-cKI reduced STS's anti-tumor efficacy (Figure 2P-2T).

### 509 **USP7 inhibited RBPJ ubiquitination**

510 Since USP7 is a deubiquitinase [36], we conducted immunoprecipitation-MS assays to identify its  
511 substrate affecting T cell function. Our analysis revealed an absence of binding between USP7 and PD1  
512 (Figure 3A). Consequently, we sought to identify the protein whose ubiquitination degradation is  
513 inhibited by USP7 to sustain PD1 expression. We found that USP7 bound to RBPJ in CD3<sup>+</sup> T cells, a T  
514 cell exhaustion protein [37](Figure 3A), which was confirmed by earlier data [38] (Figure 3B). Our  
515 study demonstrated that *Usp7*-KO led to the inhibition of RBPJ protein expression in CD3<sup>+</sup> T cells, and  
516 *Usp7*-OE up-regulated it (Figure 3C), with no impact on its transcript levels (Figure 3D). This  
517 suggested that USP7 played a role in inhibiting the RBPJ ubiquitination in CD3<sup>+</sup> T cells. Additionally,  
518 STS, which acted upstream of USP7, was found to inhibit RBPJ expression at the translational level  
519 (Figure 3E) rather than the transcriptional level (Figure 3F) in CD3<sup>+</sup> T cells. Rescue experiments  
520 further revealed that STS diminished the expression of both USP7 and RBPJ in T cells, while *Usp7*-OE  
521 mitigated the inhibitory effect of STS on RBPJ expression (Figure 3G). Subsequently, we investigated  
522 the interaction between USP7 and RBPJ. Through immunoprecipitation and molecular docking  
523 analyses, we confirmed the interaction between them in CD3<sup>+</sup> T cells (Figure 3H, 3I). To further  
524 elucidate the binding domains, we synthesized a series of domain-deficient mutants of them (Figure 3J,  
525 3K) and discovered that the N-terminal region (NTR) of RBPJ interacted with the UBL1-5 domain of  
526 USP7 in CD3<sup>+</sup> T cells (Figure 3L, 3M).

527 We then investigated USP7's role in RBPJ protein degradation. *Usp7*-OE appeared to reduce RBPJ  
528 ubiquitination in CD3<sup>+</sup> T cells (Figure 3N), while its absence increased it (Figure 3O). The NTR of  
529 RBPJ was crucial for complex formation, and its deletion boosted RBPJ ubiquitination in CD3<sup>+</sup> T cells  
530 (Figure 3P). The AXXPXAXAP motif is key for DUB recognition in RBPJ [39], and removing it was

531 found to enhance RBPJ ubiquitination in CD3<sup>+</sup> T cells (Figure 3Q). The UBL1-5 domain of USP7 was  
532 also essential for binding, and its absence increased RBPJ ubiquitination in CD3<sup>+</sup> T cells (Figure 3R). It  
533 has been reported that the DUB domain binds ubiquitin [36], and its absence was shown to increase  
534 RBPJ ubiquitination in CD3<sup>+</sup> T cells (Figure 3S). Finally, we indicated that overexpressing *Usp7*, while  
535 using Cycloheximide to accelerate protein degradation, slowed RBPJ degradation in CD3<sup>+</sup> T cells  
536 (Figure 3T).

### 537 **USP7 aggravated T cell exhaustion by up-regulating RBPJ**

538 We analyzed the effect of *Rbpj*-cKO on HCC and revealed it inhibited tumor growth (Figure 4A-4D)  
539 and improved prognosis (Figure 4E). Mass cytometry was performed to detail *Rbpj*-cKO's regulatory  
540 effect on T cells. NMDS analysis indicated that *Rbpj*-cKO significantly changed T cell function (Figure  
541 4F). Hierarchical clustering heatmap identified 13 T cell subsets (Figure S4A), including IL7R<sup>+</sup> γδT  
542 cells, IL12<sup>+</sup> GZMB<sup>+</sup> γδT cells, CD69<sup>+</sup> TCF7<sup>+</sup> CD4<sup>+</sup> T cells, CD95<sup>+</sup> TOX<sup>+</sup> CD8<sup>+</sup> T cells, IL2<sup>+</sup> CD27<sup>+</sup>  
543 CD4<sup>+</sup> T cells, IL12<sup>+</sup> CD44<sup>+</sup> CD4<sup>+</sup> T cells, KI67<sup>+</sup> TCF7<sup>+</sup> CD4<sup>+</sup> T cells, CD95<sup>+</sup> CD39<sup>+</sup> CD8<sup>+</sup> T cells,  
544 TBET<sup>+</sup> CD69<sup>+</sup> CD4<sup>+</sup> T cells, IL2<sup>+</sup> TBET<sup>+</sup> γδT cells, TCF7<sup>+</sup> CD69<sup>+</sup> CD8<sup>+</sup> T cells, TNFA<sup>+</sup> TCF7<sup>+</sup> CD8<sup>+</sup>  
545 T cells, and IL2<sup>+</sup> CD27<sup>+</sup> CD8<sup>+</sup> T cells (Figure 4G). Post-*Rbpj*-cKO, IL12<sup>+</sup> GZMB<sup>+</sup> γδT cells, CD69<sup>+</sup>  
546 TCF7<sup>+</sup> CD4<sup>+</sup> T cells, IL2<sup>+</sup> CD27<sup>+</sup> CD4<sup>+</sup> T cells, IL12<sup>+</sup> CD44<sup>+</sup> CD4<sup>+</sup> T cells, KI67<sup>+</sup> TCF7<sup>+</sup> CD4<sup>+</sup> T  
547 cells, TBET<sup>+</sup> CD69<sup>+</sup> CD4<sup>+</sup> T cells, IL2<sup>+</sup> TBET<sup>+</sup> γδT cells, TCF7<sup>+</sup> CD69<sup>+</sup> CD8<sup>+</sup> T cells, IL2<sup>+</sup> CD27<sup>+</sup>  
548 CD8<sup>+</sup> T cells, and TNFA<sup>+</sup> TCF7<sup>+</sup> CD8<sup>+</sup> T cells increased, while CD95<sup>+</sup> TOX<sup>+</sup> CD8<sup>+</sup> T cells, CD95<sup>+</sup>  
549 CD39<sup>+</sup> CD8<sup>+</sup> T cells, and IL7R<sup>+</sup> γδT cells decreased (Figure 4H, 4I). Moreover, *Rbpj*-cKO appeared to  
550 increase CD3<sup>+</sup> T cell infiltration and inhibited two exhaustion genes (CTLA4 and TOX) expression in  
551 CD4<sup>+</sup> T cells and five exhaustion genes (CD39, CTLA4, PD1, TOX, and VISTA) expression in CD8<sup>+</sup>  
552 T cells (Figure S4B). It also increased the expression of IL21 in CD4<sup>+</sup> or CD8<sup>+</sup> T cells and KI67 in  
553 CD4<sup>+</sup> T cells (Figure S4B). What's more, *Usp7*-cKI was witnessed to reduce the antitumor efficacy of



554 *Rbpj*-cKO (Figure 4J-4N), and *Rbpj*-cKI rescued the tumor reduction phenotype under STS treatment  
555 (Figure 4O-4S).

### 556 **RBPJ enhanced transcription of exhaustion genes**

557 Given that Notch1 causes T cell failure [40], we evaluated RBPJ's dependence on Notch1 for T cell  
558 regulation. Notch signaling inhibitors MK-0752 and Avagacestat alleviated T cell exhaustion, and  
559 *Rbpj*-cKO further reduced exhaustion gene expression in T cells (Figure S5A), suggesting that RBPJ-  
560 induced exhaustion was not entirely dependent on Notch1. To explore RBPJ's role in T cell exhaustion,  
561 we analyzed its DNA binding and discovered that RBPJ was bound to transcription start sites and  
562 promoters in CD3<sup>+</sup> T cells (Figure 5A, 5B), including Notch pathway target gene *Ccnd3*, etc. (Figure  
563 S5B). KEGG analysis indicated that T cell- or HCC-related items like "T-cell leukemia virus 1  
564 infection", "Hepatocellular carcinoma", "T cell receptor signaling pathway", "PD-L1 expression and  
565 PD-1 checkpoint pathway in cancer", and "Th1 and Th2 cell differentiation" were up-regulated at  
566 RBPJ enrichment peaks (Figure 5C). To identify the target of RBPJ induced exhaustion, we integrated  
567 RBPJ enrichment peaks, transcripts downregulated by *Rbpj*-cKO, and known T cell exhaustion genes  
568 [41], revealing *Irf4* [10] and *Tnfrsf1b* [11] as targets (Figure 5D-5F). DNA pull-down assay confirmed  
569 RBPJ's presence on their promoters in CD3<sup>+</sup> T cells (Figure 5G). JASPAR [42] predicted RBPJ bound  
570 to TGGGAA of the *Irf4* promoter and TTACCA of the *Tnfrsf1b* promoter, with mutations at these sites  
571 inhibiting their binding in CD3<sup>+</sup> T cells (Figure 5H). *Rbpj*-cKO appeared to reduce expression of both  
572 genes in CD3<sup>+</sup> T cells (Figure 5I, 5J). Furthermore, overexpression of *Irf4* and *Tnfrsf1b* in CD3<sup>+</sup> T cells  
573 reduced the protective effect of *Rbpj*-cKO, indicating RBPJ induced T cell exhaustion through them  
574 (Figure 5K, S5C).

575 We noted that KI67 expression increased with STS, *Usp7*-cKO, or *Rbpj*-cKO, but RBPJ didn't affect  
576 proliferation-related gene transcription (Figure 5D). Given RBPJ's involvement in chromatin  
577 conformation and genome transcription via histone H3 modification [43], we analyzed 22 histone H3

578 modifications, and found H3cit, H3K36me1, H3K36me3, H3K9ac, H3K4me1, H3K4me3, H3K9me2,  
579 H3K27me1, H3K79me1, H3K79me3, H3K27ac, and H3S10P levels were elevated after *Rbpj*-cKO,  
580 with H3Ser10P (associated with mitotic chromosome condensation [44]) being the most significant.  
581 Moreover, *Rbpj*-cKO was found to increased H3Ser10P expression in CD3<sup>+</sup> T cells (Figure 5M, 5N),  
582 and the G2/M phase rise caused by *Rbpj*-cKO was reversed by SB-747651A, a H3S10P phosphorylase  
583 MSK1 [45] inhibitor (Figure 5O). Thus, RBPI functioned as a transcription factor and chromatin  
584 regulator, worsening T cell function and hindering proliferation.

### 585 **USP7 underwent UFMylation**

586 In view of STS inhibiting the expression of USP7 from translation, we employed immunoprecipitation-  
587 MS assays to identify proteins interacting with USP7. USP7 was presented to interact with the  
588 UFMylation E3 ligase UFL1 in CD3<sup>+</sup> T cells [5] (Figure 3A, 6A), suggesting USP7's involvement in  
589 UFMylation. We found that although altering *Ufl1* or *Ufsp2* [5] didn't affect USP7 transcripts (Figure  
590 6B), *Ufl1* increased USP7 protein levels (Figure 6C, 6D), and *Ufsp2* decreased them in CD3<sup>+</sup> T cells  
591 (Figure 6E, 6F). Therefore, we believed that USP7 undergoes UFMylation. To explore USP7  
592 UFMylation's molecular mechanism, we examined the binding of UFM1 [5], UFL1, and UFSP2 each  
593 to USP7. Immunoprecipitation and molecular docking revealed that USP7 bound to UFL1, UFM1, and  
594 UFSP2 in CD3<sup>+</sup> T cells (Figure 6G-6L). To pinpoint the binding regions, we created domain-deficient  
595 mutants of them (Figure 6M-6O) and discovered that USP7's C-terminal region (CTR) was bound to  
596 UFL1's CTR (Figure 6P, 6Q) and UFM1's Ufm1 domain in CD3<sup>+</sup> T cells (Figure 6R, 6S).  
597 Additionally, USP7's UUB domain and CTR interacted with UFSP2's NTR in CD3<sup>+</sup> T cells (Figure  
598 6T, 6U).

### 599 **STS inhibited USP7 UFMylation thus increasing its ubiquitination**

600 Since USP7 underwent UFMylation, we assessed STS's impact on it and found that STS inhibited  
601 USP7 UFMylation in CD3<sup>+</sup> T cells (Figure 7A), whereas refeed enhanced it (Figure 7B). UFL1 is

known to stabilize substrates via UFMylation [5], prompting us to investigate its effect on USP7. We demonstrated that UFL1 enhanced USP7 UFMylation in CD3<sup>+</sup> T cells (Figure 7C). The inactive UFM1 form, achieved by removing the last three C-terminal amino acids (83Gly-Ser-Cys85, ΔC3) [46], effectively stopped USP7 UFMylation (Figure 7C). Furthermore, UFL1 enhanced USP7 UFMylation and reduced its ubiquitination in CD3<sup>+</sup> T cells (Figure 7D, 7E), while UFSP2 decreased USP7 UFMylation and increased its ubiquitination (Figure 7F, 7G).

Furthermore, we examined USP7 ubiquitination by creating lysine (K)-arginine (R) mutants of potential sites from PhosphoSitePlus [47]. Only K1097R stopped USP7 ubiquitination in CD3<sup>+</sup> T cells (Figure 7H), and this site was highly conserved across species (Figure 7I). Moreover, *Ufl1*-OE enhanced USP7 protein stability in CD3<sup>+</sup> T cells (Figure 7J). Finally, we mutated ubiquitin's K to R, finding K48R inhibited USP7 ubiquitination in CD3<sup>+</sup> T cells (Figure 7K), while *Ufl1* reduced K48-linked its ubiquitination (Figure 7L).

#### **STS inhibited CD36 N-glycosylation and thus preventing USP7 UFMylation**

Since STS limits glucose intake [48] and reduces N-glycosylation [49], and energy inductor AMPK inhibits PD1 UFMylation [29], we proposed that STS regulates USP7 UFMylation to alleviate T cell exhaustion by limiting N-glycosylation of AMPK-associated proteins. Earlier data [50] revealed that CD36, INSR, and HMGCR, related to the AMPK pathway, might undergo N-glycosylation (Figure 8A). We found that *Cd36*-OE reduced p-AMPK/AMPK levels in CD3<sup>+</sup> T cells (Figure 8B), while its deletion did the opposite (Figure 8C). However, HMGCR and INSR deletions didn't impact AMPK phosphorylation in CD3<sup>+</sup> T cells (Figure S6A). Therefore, we hypothesized that CD36 is N-glycosylated and that this modification affects AMPK phosphorylation and USP7 UFMylation. We then used three N-glycosylation inhibitors Tunicamycin, PNGase F, and Swainsonine on CD3<sup>+</sup> T cells, which reduced CD36's molecular weight in CD3<sup>+</sup> T cells (Figure 8D), confirming that the higher molecular weight form was indeed N-glycosylated CD36. Additionally, glucose starvation maintained

CD36's higher molecular weight (Figure 8D). We then investigated CD36 N-glycosylation sites and identified N320, N321, and N417 as potential sites through the earlier data [50, 51] (Figure 8E). Simultaneous mutations at three sites (3Q) appeared to be necessary to suppress CD36 N-glycosylation in CD3<sup>+</sup> T cells (Figure 8F). Furthermore, we investigated how CD36 N-glycosylation affects its membrane localization and expression, finding that N-glycosylation inhibitors, glucose starvation, or 3Q of CD36 impaired CD36 membrane localization (Figure 8G, S6B, S6C) without altering its expression (Figure S6D, S6E) in CD3<sup>+</sup> T cells. Furthermore, 3Q of CD36 increased p-AMPK/AMPK levels in CD3<sup>+</sup> T cells (Figure 8H). Using the AMPK inhibitor Dorsomorphine and the agonist A-769662 on CD3<sup>+</sup> T cells, we observed that Dorsomorphine increased USP7's binding to UFL1 (Figure 8I), whereas A-769662 decreased it (Figure 8J). This led us to hypothesize that CD36 N-glycosylation restricts USP7 UFMylation by blocking AMPK phosphorylation. As expected, *Cd36*-OE enhanced USP7's binding to UFL1 in CD3<sup>+</sup> T cells (Figure 8K), whereas *Cd36*-KO or 3Q of CD36 prevented this interaction (Figure 8L, 8M). Finally, 3Q inhibited USP7 UFMylation and increased its ubiquitination in CD3<sup>+</sup> T cells, a process blocked by Dorsomorphine (Figure 8N).

#### **STS improved the immunotherapy efficacy of immunotherapy**

Furthermore, given that STS had the potential to mitigate T cell exhaustion, we investigated its clinical significance and its synergistic value when combined with immune checkpoint inhibitors (ICIs) in conversion therapy. We constructed PDOX models and treated them with anti-PD1 and anti-CTLA4 antibodies combined with STS. We observed that both two ICIs and STS inhibited HCC growth (Figure S7A, S7B) and downregulated the expression of exhaustion genes PD1, TOX and TIGIT (Figure S7C, S7D). Meanwhile, STS enhanced two ICIs' effect on exhaustion gene expression suppression (Figure S7D). Both inhibitors also enhanced the therapeutic effect of STS (Figure S7D). Notably, while STS resulted in a 20% reduction of PD1 expression on CD4<sup>+</sup> T cells, it achieved a 40% reduction on CD8<sup>+</sup> T cells (Figure S7D). This observation aligned with the view suggesting that STS

650 significantly impacted tumor-infiltrating CD8<sup>+</sup> T cells rather than CD4<sup>+</sup> T cells (Figure S1B). Finally,  
651 to evaluate the clinical relevance of USP7 or RBPJ expression and HCC immunotherapy response, we  
652 calculated the TIDE scores for the high and low expression groups of them. Our results showed that the  
653 low expression levels of these two reflected a more ideal treatment response rate (Figure S7E).

## 654 **Discussion**

655 Energy metabolism regulates T cell differentiation, colonization, circulation, and response [52-54].  
656 Memory T cells in bone marrow are resting cells adapted for long-term survival with limited nutrients  
657 [52]. Intermittent fasting influences T cell proliferation, with 8-week mild fasting boosting naive CD4<sup>+</sup>  
658 T cell growth [53]. A restrictive diet also reduces the expression of T cell exhaustion genes like PD1,  
659 TIM3, and KLRG1 [54]. This suggests that there is a complex interaction between STS and T cell  
660 function that needs further study. Our study showed that STS boosted T cell effector function,  
661 cytotoxicity, proliferation, and prevented exhaustion, thereby enhancing anti-tumor immunity. We  
662 connected N-glycosylation, UFMylation, and ubiquitination to metabolic/immune responses,  
663 highlighting that regulation of these PTMs was crucial for developing effective T cell functions under  
664 low glucose conditions.

665 UFMylation is crucial in immunotherapy [5], and targeting it could improve treatment outcomes  
666 [30]. As a significant PTMs, UFMylation offers a promising approach for cancer therapy [30]. In  
667 addition, the immune system is vital for controlling tumor growth, with T-cell-based therapies like ICI  
668 and CAR T-cell therapy being key cancer treatments [29]. This study highlighted the importance of  
669 UFMylation in T cells, in regulating T cell activation and anti-tumor immunity. Previous studies  
670 indicated that eliminating PIRIN UFMylation induces ferroptosis of macrophages and boosts M1-type  
671 differentiation [55]. Inhibiting PD1 UFMylation enhances T cell cytotoxicity [29]. What's more,  
672 disrupting 14-3-3ε UFMylation activates antiviral responses and induces the expression of the  
673 interferon gene [56]. In this study, we discovered that USP7 UFMylation prevented its ubiquitination,

674 stabilized it, and aggravated T cell exhaustion. Therefore, the inhibition of UFMylation is indeed a key  
675 strategy for improving T cell function.

676 PTMs of transcription factors intricately interact with immune and inflammatory responses [57-59].  
677 Specifically, IRF3 up-regulates the expression of the ISGylation effector ISG15 while significantly  
678 downregulating thermogenic gene expression, a crucial mechanism through which inflammation  
679 suppresses adipose tissue thermogenesis [57]. Furthermore, the ubiquitination pathway facilitates the  
680 activation of NF- $\kappa$ B signaling by promoting the phase separation of NEMO [58]. Additionally,  
681 TRIM7/RNF90 enhances autophagy during infection by modulating the ubiquitination of ATG7 [59].  
682 Our research underscored that the ubiquitination of the transcription factor RBPJ aggravated T cell  
683 exhaustion by stabilizing its expression. Furthermore, the interplay among PTMs is significant [60].  
684 This interaction is essential for accurate gene expression, maintenance of genome architecture,  
685 regulation of cell division, and the cellular response to DNA damage [60]. Our research demonstrated  
686 that USP7 UFMylation suppressed its ubiquitination, subsequently inhibiting RBPJ ubiquitination. This  
687 finding underscored the intricate relationship between ubiquitination and UFMylation.

688 We acknowledged the potential limitations inherent in this study. Firstly, the PDOX model relies on  
689 the sensitivity of the patients used to construct the model to ICIs, which may not fully account for the  
690 TME in patients who exhibit insensitivity to these inhibitors. Considering this limitation, subsequent  
691 direct testing in human patients will be essential. Secondly, the dual KO of USP7 and RBPJ  
692 theoretically raises concerns regarding genotoxicity. Lastly, for clinical applications, it is imperative to  
693 recognize that if the elimination of USP7/RBPJ dual-edited cells is compromised, the resultant  
694 accumulation of a substantial number of highly proliferative and cytotoxic T cells could significantly  
695 elevate the risk of T cell lymphoma and cytokine storm. This issue can be mitigated through dose  
696 escalation studies and by incorporating STS to reduce the dosage. Considering these uncertainties, the  
697 preliminary clinical trials for this strategy should evaluate the application of gene therapy utilizing  
698 USP7/RBPJ dual-edited cells at comparatively low concentrations.

699 **Conclusions**

700 Our study found that STS disrupted CD36 N-glycosylation, activated AMPK phosphorylation, reduced  
701 USP7 UFMylation, enhanced its ubiquitination, and destabilized USP7. This led to increased RBPJ  
702 ubiquitination and degradation, inhibiting the IRF4/TNFRSF1B axis and alleviating T cell exhaustion  
703 (Figure 8O). Our study highlighted the role of N-glycosylation, UFMylation, and ubiquitin in  
704 regulating T cell anti-tumor immunity.

705  
706 **Abbreviations**

707 MS: mass spectrometry; cKI: conditional knock-in; cKO: conditional knockout; CTR: C-terminal  
708 region; CyTOF: cytometry by time-of-flight; FDR: false discovery rate; HCC: hepatocellular  
709 carcinoma; ICI: immune checkpoint inhibitor; *i.p.*: intraperitoneally; LC-MS: liquid chromatography-  
710 mass spectrometry; MS, mass spectrometry; NMDS: non-metric Multidimensional Scaling; NTR: N-  
711 terminal region; OE: overexpression; PDOX: patient-derived orthotopic xenograft; PTMs: protein  
712 translational modifications; RT: room temperature; STS: short-term starvation; TME: tumor  
713 microenvironment; WT: wild-type.

714  
715 **Acknowledgments**

716 This study was funded by grants from the National Natural Science Foundation of China (82372936);  
717 Fujian Provincial Health Technology Project (2022CXA009); Joint Funds Project for Innovation of  
718 Science and Technology, Fujian province (2021Y9067); High-Level Medical Care Construction  
719 Foundation of Fujian Province ([2021]76).

720 **Author Contributions**

721 B.L.P, S.Y.C and H.W developed the study concept; X.Q.W and N.H.T supervised the project; B.L.P,  
722 S.Y.C, H.W and X.X.Z conducted the experiments; B.L.P, S.Y.C, Z.Z, D.J.Y, Y.X.Y, Y.L and X.Y.Z

723 performed the data analysis and wrote the manuscript. All the authors have read and approved the final  
724 version of the manuscript.

## 725 **Competing Interests**

726 The authors have declared that there is no competing.

## 727 **Data availability**

728 The raw mass spectrometry data, mass cytometry data, or sequencing data that support the findings of  
729 this study are deposited in PRJCA032925 (proteomics,  
730 <https://ngdc.cncb.ac.cn/bioproject/browse/PRJCA032925>), PRJCA032826 (mass cytometry,  
731 <https://ngdc.cncb.ac.cn/bioproject/browse/PRJCA032826>), CRA020880 (CUT&Tag,  
732 <https://ngdc.cncb.ac.cn/gsa/browse/CRA020880>, CRA020866 (RNA-seq,  
733 <https://ngdc.cncb.ac.cn/gsa/browse/CRA020866>), and PRJCA033025 (Immunoprecipitation-MS,  
734 <https://ngdc.cncb.ac.cn/bioproject/browse/PRJCA033025>).

735

## 736 **References**

- 737 1. Kim KH, Kim YH, Son JE, Lee JH, Kim S, Choe MS, et al. Intermittent fasting promotes adipose thermogenesis  
738 and metabolic homeostasis via VEGF-mediated alternative activation of macrophage. *Cell Res.* 2017; 27: 1309-26.  
739 2. Jordan S, Tung N, Casanova-Acebes M, Chang C, Cantoni C, Zhang D, et al. Dietary Intake Regulates the  
740 Circulating Inflammatory Monocyte Pool. *Cell.* 2019; 178: 1102-14.e17.  
741 3. Janssen H, Kahles F, Liu D, Downey J, Koekkoek LL, Roudko V, et al. Monocytes re-enter the bone marrow  
742 during fasting and alter the host response to infection. *Immunity.* 2023; 56: 783-96.e7.  
743 4. Jiang GM, Tan Y, Wang H, Peng L, Chen HT, Meng XJ, et al. The relationship between autophagy and the  
744 immune system and its applications for tumor immunotherapy. *Mol Cancer.* 2019; 18: 17.  
745 5. Gerakis Y, Quintero M, Li H, Hetz C. The UFMylation System in Proteostasis and Beyond. *Trends Cell Biol.*  
746 2019; 29: 974-86.  
747 6. Tatsumi K, Yamamoto-Mukai H, Shimizu R, Waguri S, Sou YS, Sakamoto A, et al. The Ufm1-activating enzyme  
748 Uba5 is indispensable for erythroid differentiation in mice. *Nat Commun.* 2011; 2: 181.  
749 7. Liu J, Wang Y, Song L, Zeng L, Yi W, Liu T, et al. A critical role of DDRGK1 in endoplasmic reticulum  
750 homeostasis via regulation of IRE1 $\alpha$  stability. *Nat Commun.* 2017; 8: 14186.  
751 8. Qin B, Yu J, Nowsheen S, Wang M, Tu X, Liu T, et al. UFL1 promotes histone H4 ufmylation and ATM  
752 activation. *Nat Commun.* 2019; 10: 1242.  
753 9. Balce DR, Wang YT, McAllaster MR, Dunlap BF, Orvedahl A, Hykes BL, Jr., et al. UFMylation inhibits the  
754 proinflammatory capacity of interferon- $\gamma$ -activated macrophages. *Proc Natl Acad Sci U S A.* 2021; 118.  
755 10. Man K, Gabriel SS, Liao Y, Gloury R, Preston S, Henstridge DC, et al. Transcription Factor IRF4 Promotes  
756 CD8(+) T Cell Exhaustion and Limits the Development of Memory-like T Cells during Chronic Infection. *Immunity.* 2017;  
757 47: 1129-41.e5.  
758 11. Gao Y, Shi H, Zhao H, Yao M, He Y, Jiang M, et al. Single-cell transcriptomics identify TNFRSF1B as a novel T-  
759 cell exhaustion marker for ovarian cancer. *Clin Transl Med.* 2023; 13: e1416.  
760 12. Nyberg WA, Ark J, To A, Clouden S, Reeder G, Muldoon JJ, et al. An evolved AAV variant enables efficient  
761 genetic engineering of murine T cells. *Cell.* 2023; 186: 446-60.e19.



13. Ajona D, Ortiz-Espinosa S, Lozano T, Exposito F, Calvo A, Valencia K, et al. Short-term starvation reduces IGF-1 levels to sensitize lung tumors to PD-1 immune checkpoint blockade. *Nat Cancer*. 2020; 1: 75-85.
14. Chen S, Zhou Y, Chen Y, Gu J. fastp: an ultra-fast all-in-one FASTQ preprocessor. *Bioinformatics*. 2018; 34: i884-i90.
15. Ramírez F, Ryan DP, Grüning B, Bhardwaj V, Kilpert F, Richter AS, et al. deepTools2: a next generation web server for deep-sequencing data analysis. *Nucleic Acids Res*. 2016; 44: W160-5.
16. Zhang Y, Liu T, Meyer CA, Eeckhoutte J, Johnson DS, Bernstein BE, et al. Model-based analysis of ChIP-Seq (MACS). *Genome Biol*. 2008; 9: R137.
17. Yu G, Wang LG, He QY. ChIPseeker: an R/Bioconductor package for ChIP peak annotation, comparison and visualization. *Bioinformatics*. 2015; 31: 2382-3.
18. Tu S, Li M, Chen H, Tan F, Xu J, Waxman DJ, et al. MANorm2 for quantitatively comparing groups of ChIP-seq samples. *Genome Res*. 2021; 31: 131-45.
19. Robinson JT, Thorvaldsdottir H, Turner D, Mesirov JP. igv.js: an embeddable JavaScript implementation of the Integrative Genomics Viewer (IGV). *Bioinformatics*. 2023; 39.
20. Finck R, Simonds EF, Jager A, Krishnaswamy S, Sachs K, Fantl W, et al. Normalization of mass cytometry data with bead standards. *Cytometry A*. 2013; 83: 483-94.
21. Hahne F, LeMeur N, Brinkman RR, Ellis B, Haaland P, Sarkar D, et al. flowCore: a Bioconductor package for high throughput flow cytometry. *BMC Bioinformatics*. 2009; 10: 106.
22. Finak G, Jiang W, Pardo J, Asare A, Gottardo R. QUALiFiER: an automated pipeline for quality assessment of gated flow cytometry data. *BMC Bioinformatics*. 2012; 13: 252.
23. Bendall SC, Simonds EF, Qiu P, Amir el AD, Krutzik PO, Finck R, et al. Single-cell mass cytometry of differential immune and drug responses across a human hematopoietic continuum. *Science*. 2011; 332: 687-96.
24. Van Gassen S, Callebaut B, Van Helden MJ, Lambrecht BN, Demeester P, Dhaene T, et al. FlowSOM: Using self-organizing maps for visualization and interpretation of cytometry data. *Cytometry A*. 2015; 87: 636-45.
25. Cieslak MC, Castelfranco AM, Roncalli V, Lenz PH, Hartline DK. t-Distributed Stochastic Neighbor Embedding (t-SNE): A tool for eco-physiological transcriptomic analysis. *Mar Genomics*. 2020; 51: 100723.
26. Wiśniewski JR, Zougman A, Nagaraj N, Mann M. Universal sample preparation method for proteome analysis. *Nature methods*. 2009; 6: 359-62.
27. Feng J, Ding C, Qiu N, Ni X, Zhan D, Liu W, et al. Firmiana: towards a one-stop proteomic cloud platform for data processing and analysis. *Nature biotechnology*. 2017; 35: 409-12.
28. Laskowski RA, Swindells MB. LigPlot+: multiple ligand-protein interaction diagrams for drug discovery. *J Chem Inf Model*. 2011; 51: 2778-86.
29. He C, Xing X, Chen HY, Gao M, Shi J, Xiang B, et al. UFL1 ablation in T cells suppresses PD-1 UFMylation to enhance anti-tumor immunity. *Mol Cell*. 2024; 84: 1120-38.e8.
30. Jing Y, Mao Z, Chen F. UFMylation System: An Emerging Player in Tumorigenesis. *Cancers (Basel)*. 2022; 14.
31. Alidadi M, Banach M, Guest PC, Bo S, Jamialahmadi T, Sahebkar A. The effect of caloric restriction and fasting on cancer. *Semin Cancer Biol*. 2021; 73: 30-44.
32. Dai X, Bu X, Gao Y, Guo J, Hu J, Jiang C, et al. Energy status dictates PD-L1 protein abundance and anti-tumor immunity to enable checkpoint blockade. *Mol Cell*. 2021; 81: 2317-31.e6.
33. Wang N, Wang B, Maswikiti EP, Yu Y, Song K, Ma C, et al. AMPK-a key factor in crosstalk between tumor cell energy metabolism and immune microenvironment? *Cell Death Discov*. 2024; 10: 237.
34. Ravichandran R, Kodali K, Peng J, Potts PR. Regulation of MAGE-A3/6 by the CRL4-DCAF12 ubiquitin ligase and nutrient availability. *EMBO Rep*. 2019; 20: e47352.
35. Wang Z, Kang W, Li O, Qi F, Wang J, You Y, et al. Abrogation of USP7 is an alternative strategy to downregulate PD-L1 and sensitize gastric cancer cells to T cells killing. *Acta Pharm Sin B*. 2021; 11: 694-707.
36. Park HB, Baek KH. Current and future directions of USP7 interactome in cancer study. *Biochim Biophys Acta Rev Cancer*. 2023; 1878: 188992.
37. Pan B, Wang Z, Zhang X, Shen S, Ke X, Qiu J, et al. Targeted inhibition of RBPJ transcription complex alleviates the exhaustion of CD8(+) T cells in hepatocellular carcinoma. *Commun Biol*. 2023; 6: 123.
38. Liu C, Sun L, Tan Y, Wang Q, Luo T, Li C, et al. USP7 represses lineage differentiation genes in mouse embryonic stem cells by both catalytic and noncatalytic activities. *Sci Adv*. 2023; 9: eade3888.
39. Wang X, Li Y, He M, Kong X, Jiang P, Liu X, et al. UbiBrowser 2.0: a comprehensive resource for proteome-wide known and predicted ubiquitin ligase/deubiquitinase-substrate interactions in eukaryotic species. *Nucleic Acids Res*. 2022; 50: D719-d28.
40. Gholami A. Cancer stem cell-derived exosomes in CD8(+) T cell exhaustion. *Int Immunopharmacol*. 2024; 137: 112509.
41. Zhang X, Lan Y, Xu J, Quan F, Zhao E, Deng C, et al. CellMarker: a manually curated resource of cell markers in human and mouse. *Nucleic Acids Res*. 2019; 47: D721-d8.

820 42. Rauluseviciute I, Riudavets-Puig R, Blanc-Mathieu R, Castro-Mondragon JA, Ferenc K, Kumar V, et al. JASPAR  
821 2024: 20th anniversary of the open-access database of transcription factor binding profiles. *Nucleic Acids Res.* 2024; 52:  
822 D174-d82.

823 43. Castel D, Mourikis P, Bartels SJ, Brinkman AB, Tajbakhsh S, Stunnenberg HG. Dynamic binding of RBPJ is  
824 determined by Notch signaling status. *Genes Dev.* 2013; 27: 1059-71.

825 44. Ozawa K. Reduction of phosphorylated histone H3 serine 10 and serine 28 cell cycle marker intensities after DNA  
826 damage. *Cytometry A.* 2008; 73: 517-27.

827 45. Qi H, Yang Z, Dai C, Wang R, Ke X, Zhang S, et al. STAT3 activates MSK1-mediated histone H3  
828 phosphorylation to promote NFAT signaling in gastric carcinogenesis. *Oncogenesis.* 2020; 9: 15.

829 46. Komatsu M, Chiba T, Tatsumi K, Iemura S, Tanida I, Okazaki N, et al. A novel protein-conjugating system for  
830 Ufm1, a ubiquitin-fold modifier. *Embo j.* 2004; 23: 1977-86.

831 47. Hornbeck PV, Kornhauser JM, Tkachev S, Zhang B, Skrzypek E, Murray B, et al. PhosphoSitePlus: a  
832 comprehensive resource for investigating the structure and function of experimentally determined post-translational  
833 modifications in man and mouse. *Nucleic Acids Res.* 2012; 40: D261-70.

834 48. Cahill GF, Jr. Fuel metabolism in starvation. *Annu Rev Nutr.* 2006; 26: 1-22.

835 49. Pasala C, Sharma S, Roychowdhury T, Moroni E, Colombo G, Chiosis G. N-Glycosylation as a Modulator of  
836 Protein Conformation and Assembly in Disease. *Biomolecules.* 2024; 14.

837 50. Chen X, Song X, Li J, Wang J, Yan Y, Yang F. Integrated proteomic, phosphoproteomic, and N-glycoproteomic  
838 analyses of small extracellular vesicles from C2C12 myoblasts identify specific PTM patterns in ligand-receptor  
839 interactions. *Cell Commun Signal.* 2024; 22: 273.

840 51. Hoosdally SJ, Andress EJ, Wooding C, Martin CA, Linton KJ. The Human Scavenger Receptor CD36:  
841 glycosylation status and its role in trafficking and function. *J Biol Chem.* 2009; 284: 16277-88.

842 52. Collins N, Han SJ, Enamorado M, Link VM, Huang B, Moseman EA, et al. The Bone Marrow Protects and  
843 Optimizes Immunological Memory during Dietary Restriction. *Cell.* 2019; 178: 1088-101.e15.

844 53. Ahmed T, Das SK, Golden JK, Saltzman E, Roberts SB, Meydani SN. Calorie restriction enhances T-cell-mediated  
845 immune response in adult overweight men and women. *J Gerontol A Biol Sci Med Sci.* 2009; 64: 1107-13.

846 54. Asami T, Endo K, Matsui R, Sawa T, Tanaka Y, Saiki T, et al. Long-term caloric restriction ameliorates T cell  
847 immunosenescence in mice. *Mech Ageing Dev.* 2022; 206: 111710.

848 55. Li G, Liao C, Chen J, Wang Z, Zhu S, Lai J, et al. Targeting the MCP-GPX4/HMGB1 Axis for Effectively  
849 Triggering Immunogenic Ferroptosis in Pancreatic Ductal Adenocarcinoma. *Adv Sci (Weinh).* 2024; 11: e2308208.

850 56. Snider DL, Park M, Murphy KA, Beachboard DC, Horner SM. Signaling from the RNA sensor RIG-I is regulated  
851 by ufmylation. *Proc Natl Acad Sci U S A.* 2022; 119: e2119531119.

852 57. Yan S, Kumari M, Xiao H, Jacobs C, Kochumon S, Jedrychowski M, et al. IRF3 reduces adipose thermogenesis  
853 via ISG15-mediated reprogramming of glycolysis. *J Clin Invest.* 2021; 131.

854 58. Du M, Ea CK, Fang Y, Chen ZJ. Liquid phase separation of NEMO induced by polyubiquitin chains activates NF-  
855  $\kappa$ B. *Mol Cell.* 2022; 82: 2415-26.e5.

856 59. Wang J, Qin X, Huang Y, Zhang Q, Pei J, Wang Y, et al. TRIM7/RNF90 promotes autophagy via regulation of  
857 ATG7 ubiquitination during *L. monocytogenes* infection. *Autophagy.* 2023; 19: 1844-62.

858 60. Dawson MA, Kouzarides T. Cancer epigenetics: from mechanism to therapy. *Cell.* 2012; 150: 12-27.

859

860

861

862

863

864

865

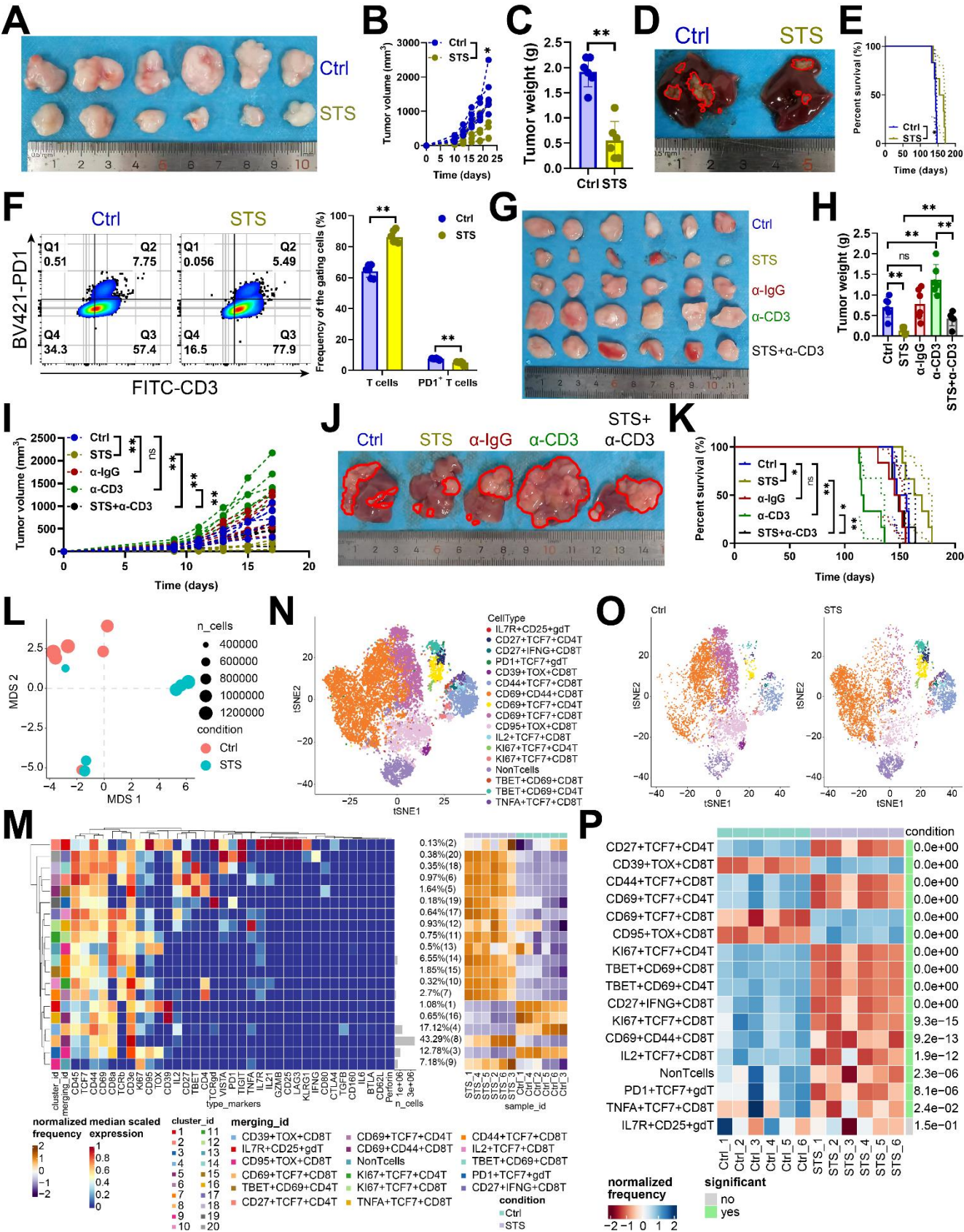


**Figure 1.** STS alleviated T cell exhaustion. (A-C) Effects of STS on subcutaneous tumor growth ( $n = 6$ ). (A) Representative. (B) Growth curve. (C) Tumor weight. (D, E) Effects of STS on primary cancer growth ( $n = 6$ ). (D) Representative. (E) Survival curve. (F) Effects of STS on T cell infiltration and its PD1 expression in primary cancer ( $n = 6$ ). (G-I) Effects of STS and neutralizing CD3<sup>+</sup> T cells on subcutaneous tumor growth ( $n = 6$ ). Anti-mouse CD3 $\epsilon$  antibody was injected into the tail vein to clear T cells. (G) Representative. (H) Growth curve. (I) Tumor weight. (J, K) Effects of STS and neutralizing CD3<sup>+</sup> T cells on primary cancer growth ( $n = 6$ ). (J) Representative. (K) Survival curve. (L) Non-metric Multidimensional Scaling analysis compared the similarity of T cell characteristic antigen expression before and after STS ( $n = 6$ ). (M) Heatmap showed the median expression of the antigen used to generate SOM ( $n = 6$ ). (N) SOM was superimposed on mass cytometry data of primary carcinoma-infiltrating T cells ( $n = 6$ ). (O) Mosaic of single T cells ( $n = 6$ ). (P) Heatmap showed the proportion of T cell subsets ( $n = 6$ ). (B), (C), (F), (H), (I), and (P) represented mean  $\pm$  SD analyzed by unpaired  $t$  test, (E) and (K) were analyzed by Log-rank test, (M) was analyzed by Euclidean Distance Clustering Algorithm. \* $P < 0.05$ , \*\* $P < 0.01$ . SOM, self-organizing map; STS, short-term starvation.



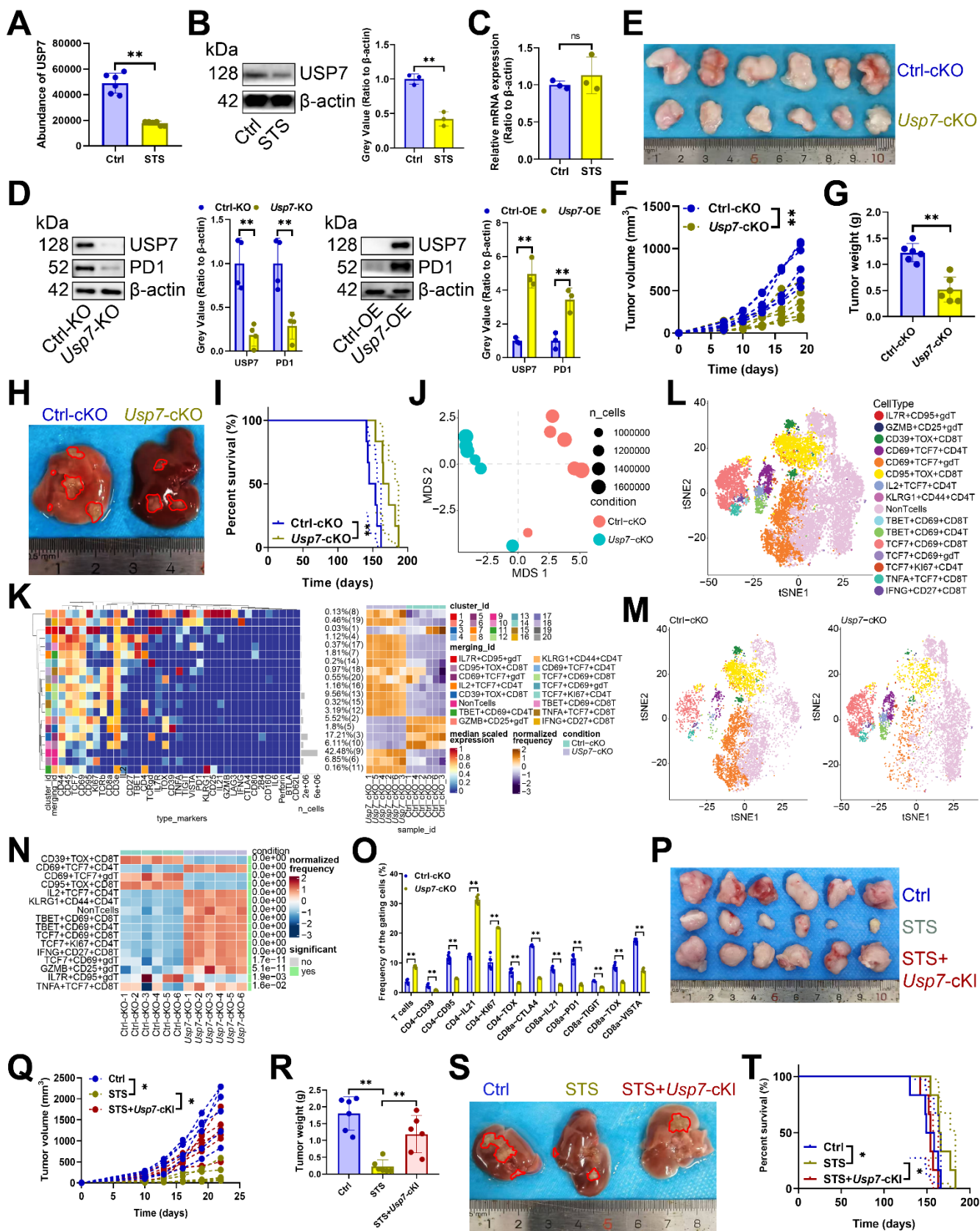


**Figure 2.** STS alleviated T cell exhaustion by inhibiting USP7. (A-C) Effects of STS on USP7 expression in primary carcinoma-infiltrating CD3<sup>+</sup> T cells were analyzed by mass spectrometry (A), immunoblotting (B) and RT-qPCR (C) (*n* = 6). (D) Effects of KO or OE of *Usp7* on PD1 expression in CD3<sup>+</sup> T cells (*n* = 6). (E-G) Effects of *Usp7*-cKO on subcutaneous tumor growth (*n* = 6). (E) Representative. (F) Growth curve. (G) Tumor weight. (H, I) Effects of *Usp7*-cKO on primary cancer growth (*n* = 6). (H) Representative. (I) Survival curve. (J) Non-metric Multidimensional Scaling analysis compared the similarity of T cell characteristic antigen expression before and after *Usp7*-cKO (*n* = 6). (K) Heatmap showed the median expression of the antigen used to generate SOM (*n* = 6). (L) SOM was superimposed on mass cytometry data of primary carcinoma-infiltrating T cells (*n* = 6). (M) Mosaic of single T cells (*n* = 6). (N) Heatmap showed the proportion of T cell subsets (*n* = 6). (O) Median expression of T cell characteristic antigen (*n* = 6). (P-R) Effects of STS and *Usp7*-cKI on subcutaneous tumor growth (*n* = 6). (P) Representative. (Q) Growth curve. (R) Tumor weight. (S, T) Effects of STS and *Usp7*-cKI on primary carcinoma growth (*n* = 6). (S) Representative. (T) Survival curve. (A-D), (F), (G), (N), (O), (Q), and (R) represented mean ± SD analyzed by unpaired *t* test, (I) and (T) were analyzed by Log-rank test, (K) was analyzed by Euclidean Distance Clustering Algorithm. \**P* <0.05, \*\**P* <0.01. cKI, conditional knock-in; cKO, conditional knockout; OE, overexpression; SOM, self-organizing map; STS, short-term starvation.

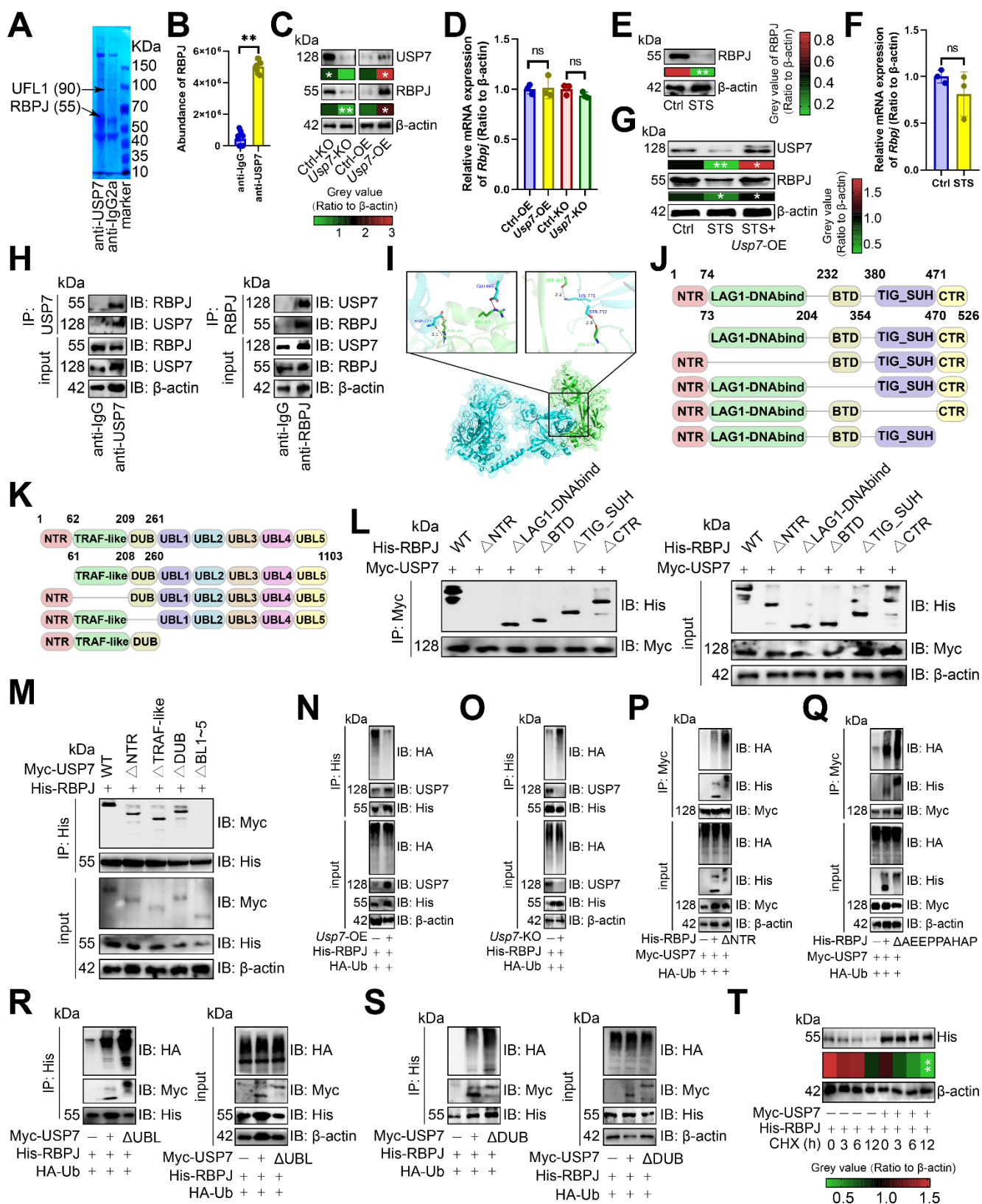


**Figure 3. USP7 inhibited RBPJ ubiquitination.** (A) Identification of proteins bound by USP7 in primary carcinoma-infiltrating CD3<sup>+</sup> T cells by immunoprecipitation-mass spectrometry assays. (B)

903 PXD039633 dataset showed the binding of USP7 and RBPJ ( $n=10$ ). (C, D) Effects of OE or KO of  
 904 *Usp7* on the expression of RBPJ protein (C) and transcript (D) in CD3<sup>+</sup> T cells ( $n=3$ ). (E, F) Effects of  
 905 STS on the expression of RBPJ protein (E) and transcript (F) in CD3<sup>+</sup> T cells ( $n=3$ ). (G) Effects of  
 906 STS and *Usp7*-OE on the RBPJ protein levels in CD3<sup>+</sup> T cells ( $n=3$ ). (H) CD3<sup>+</sup> T cell lysate was  
 907 treated with anti-IgG control and -USP7 (left) or -RBPJ (right) antibodies, with 5% lysate as input  
 908 control ( $n=3$ ). (I) Surface plot presented docking models and interface residues between USP7 (sky  
 909 blue) and RBPJ (green) proteins, hydrogen bonds highlighted with dashed lines. (J, K) Schematic plot  
 910 of domain-deficient mutants for USP7 (J) and RBPJ (K). (L, M) Immunoprecipitation identified key  
 911 domains of USP7 and RBPJ binding ( $n=3$ ). CD3<sup>+</sup> T cells were co-transfected with WT or domain-  
 912 deficient mutants (L) of Myc-labeled USP7 and His-labeled RBPJ, and vice versa (M). (N, O) Effects  
 913 of OE (N) or KO (O) of *Usp7* on RBPJ ubiquitination in CD3<sup>+</sup> T cells ( $n=3$ ). (P, Q) Effects of the  
 914 NTR (P) and AEEPPAHAP (Q) of RBPJ on its ubiquitination in CD3<sup>+</sup> T cells ( $n=3$ ). (R, S) Effect of  
 915 the UBL domain (R) and the DUB domain (S) of USP7 on RBPJ ubiquitination in CD3<sup>+</sup> T cells ( $n=$   
 916 3). (T) CD3<sup>+</sup> T cells with His-labeled RBPJ were treated with Cycloheximide, and their expression was  
 917 evaluated ( $n=3$ ). (B-G), and (T) represented mean  $\pm$  SD analyzed by unpaired  $t$  test. \* $P < 0.05$ , \*\* $P$   
 918  $< 0.01$ . KO, knockout; OE, overexpression; STS, short-term starvation; WT, wild-type.



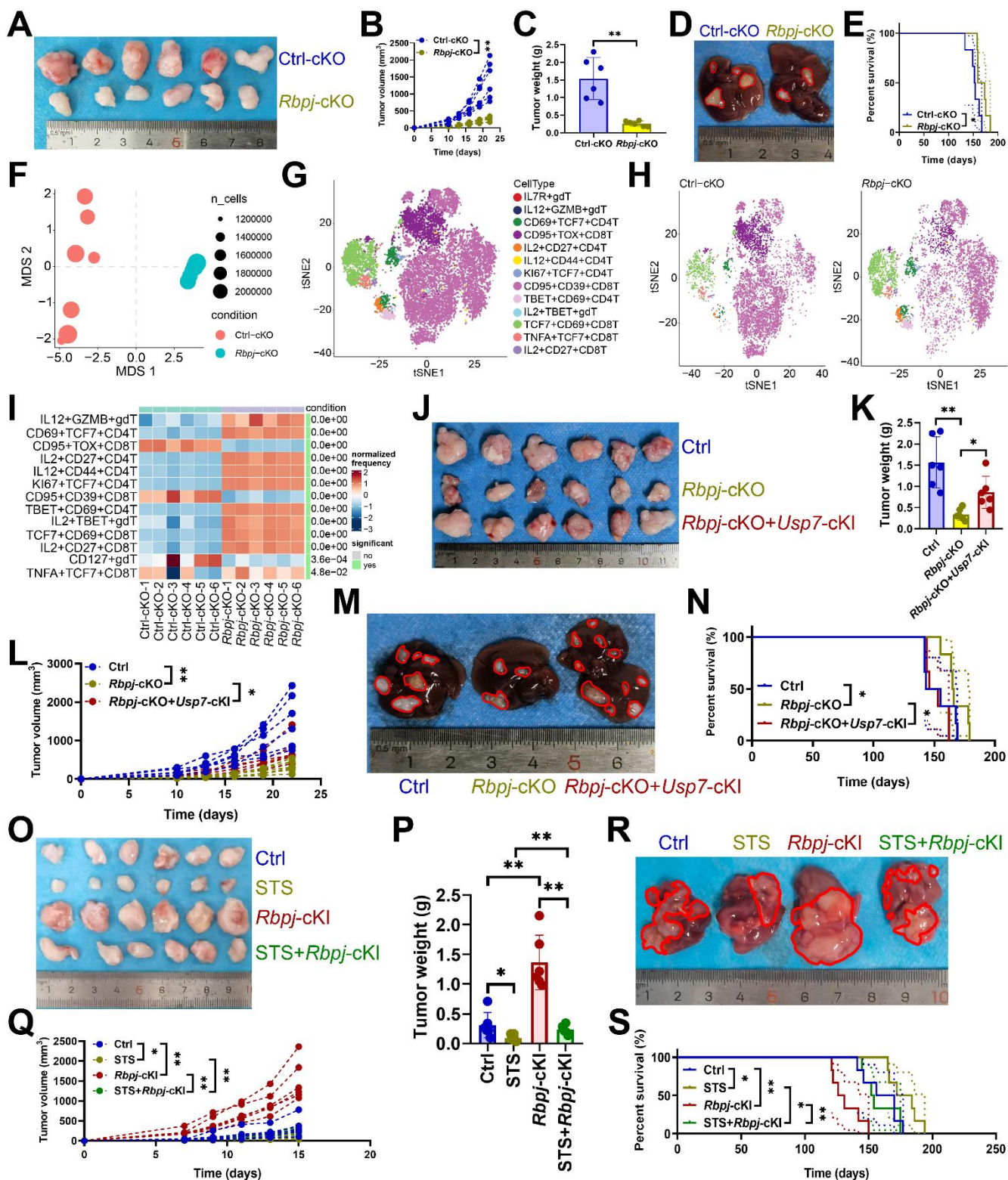


**Figure 4.** USP7 aggravated T cell exhaustion by up-regulating RBPJ. (A-C) Effects of *Rbpj*-cKO on subcutaneous tumor growth ( $n = 6$ ). (A) Representative. (B) Growth curve. (C) Tumor weight. (D, E) Effects of *Rbpj*-cKO on primary cancer growth ( $n = 6$ ). (D) Representative. (E) Survival curve. (F)

923 Non-metric Multidimensional Scaling analysis compared the similarity of T cell characteristic antigen  
924 expression before and after *Rbpj*-cKO ( $n = 6$ ). (G) SOM was superimposed on mass cytometry data of  
925 primary carcinoma-infiltrating T cells ( $n = 6$ ). (H) Mosaic map of single T cells ( $n = 6$ ). (I) Heatmap  
926 showed the proportion of T cell subsets ( $n = 6$ ). (J-L) Effects of *Rbpj*-cKO and *Usp7*-cKI on  
927 subcutaneous tumor growth ( $n = 6$ ). (J) Representative. (K) Growth curve. (L) Tumor weight. (M, N)  
928 Effects of *Rbpj*-cKO and *Usp7*-cKI on primary cancer growth ( $n = 6$ ). (M) Representative. (N) Survival  
929 curve. (O-Q) Effects of STS and *Rbpj*-cKI on subcutaneous tumor growth ( $n = 6$ ). (O) Representative.  
930 (P) Growth curve. (Q) Tumor weight. (R, S) Effects of STS and *Rbpj*-cKI on primary cancer growth ( $n$   
931  $= 6$ ). (R) Representative. (S) Survival curve. (B), (C), (I), (K), (L), (P), and (Q) represented mean  $\pm$  SD  
932 analyzed by unpaired  $t$  test, (E), (N), and (S) were analyzed by Log-rank test.  $*P < 0.05$ ,  $**P < 0.01$ .  
933 cKI, conditional knock-in; cKO, conditional knockout; SOM, self-organizing map.

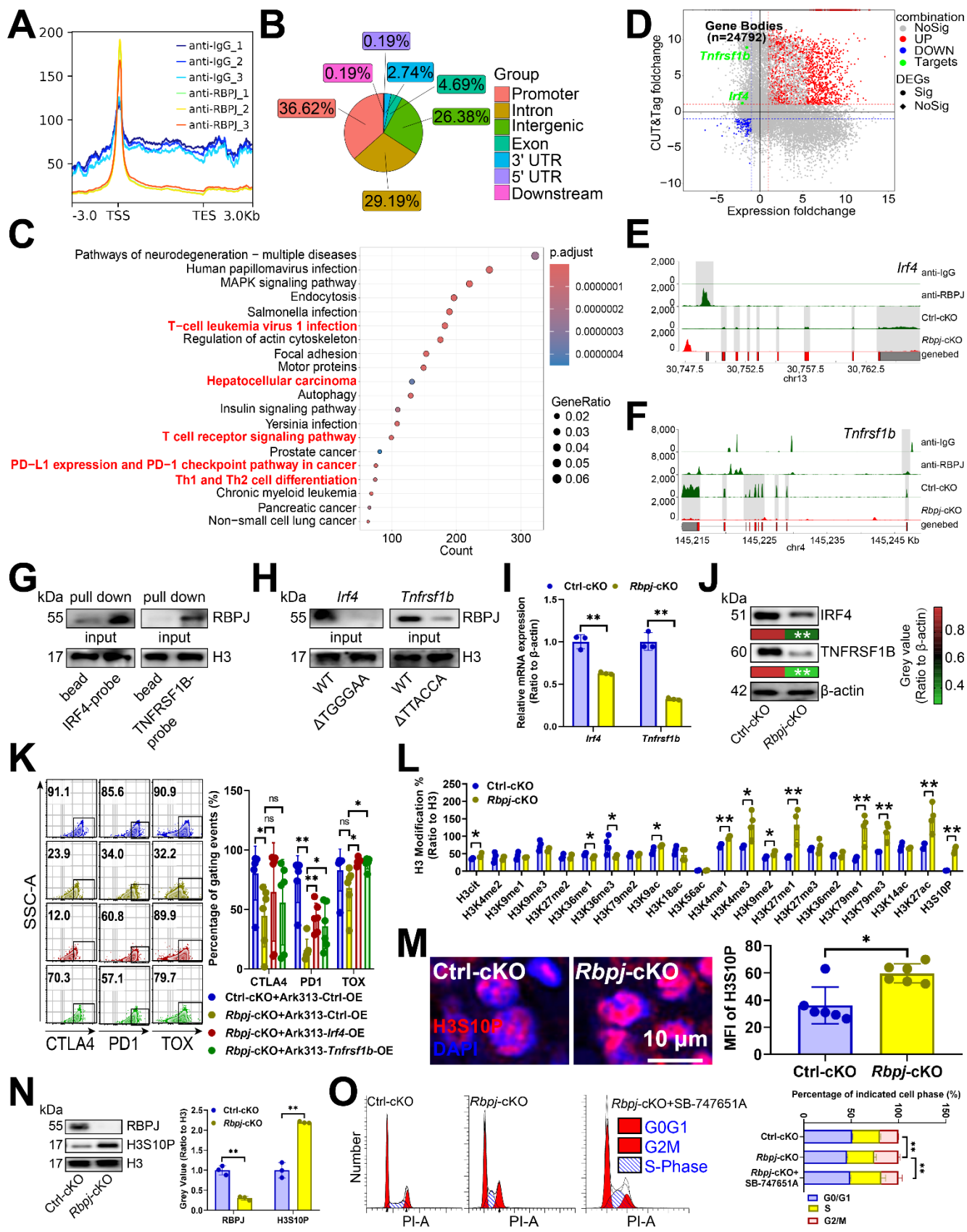


**Figure 5.** RBPJ enhanced transcription of exhaustion genes. (A, B) The cluster plot showed the DNA fragments that RBPJ binds to (A), and their distribution across the genome (B) in primary carcinoma-infiltrating CD3<sup>+</sup> T cells ( $n = 3$ ). (C) Pathway enrichment analysis of genes mapped to RBPJ-bound DNA fragments compared to IgG controls in CD3<sup>+</sup> T cells ( $n = 3$ ). Red indicated T cell- or HCC-related items. (D) A four-quadrant plot presented the distribution of genes with significant alterations in both the DNA fragment bound to RBPJ and the mRNA levels in CD3<sup>+</sup> T cells ( $n = 3$ ). (E, F) Snapshot plots showed explicit transcription expression of *Irf4* (E) and *Tnfrsf1b* (F) and the enrichment signal of RBPJ on their promoter in CD3<sup>+</sup> T cells ( $n = 3$ ). Gray indicated the differential signal. (G) DNA pull-down experiment demonstrated the binding of RBPJ to the promoter of *Irf4* or *Tnfrsf1b* in CD3<sup>+</sup> T cells ( $n = 3$ ). (H) Effects of loss of TGGGAA of *Irf4* promoter or TTACCA of *Tnfrsf1b* promoter on DNA affinity of RBPJ in CD3<sup>+</sup> T cells ( $n = 3$ ). (I, J) Effects of *Rbpj*-cKO on transcription (I) and protein (J) expression of IRF4 or TNFRSF1B in CD3<sup>+</sup> T cells ( $n = 3$ ). (K) Flow cytometry demonstrated inhibitory receptor expression in CD3<sup>+</sup> T cells ( $n = 6$ ). (L) ELISA demonstrated 22 histone H3 modification levels in CD3<sup>+</sup> T cells ( $n = 4$ ). (M, N) Immunofluorescence (M) and immunoblotting (N) demonstrated the expression of H3S10P in CD3<sup>+</sup> T cells ( $n = 3$ ). (O) Flow cytometry presented the cell cycle of CD3<sup>+</sup> T cells ( $n = 3$ ). (I-O) represented mean  $\pm$  SD analyzed by unpaired  $t$  test. \* $P < 0.05$ , \*\* $P < 0.01$ . cKO, conditional knockout.



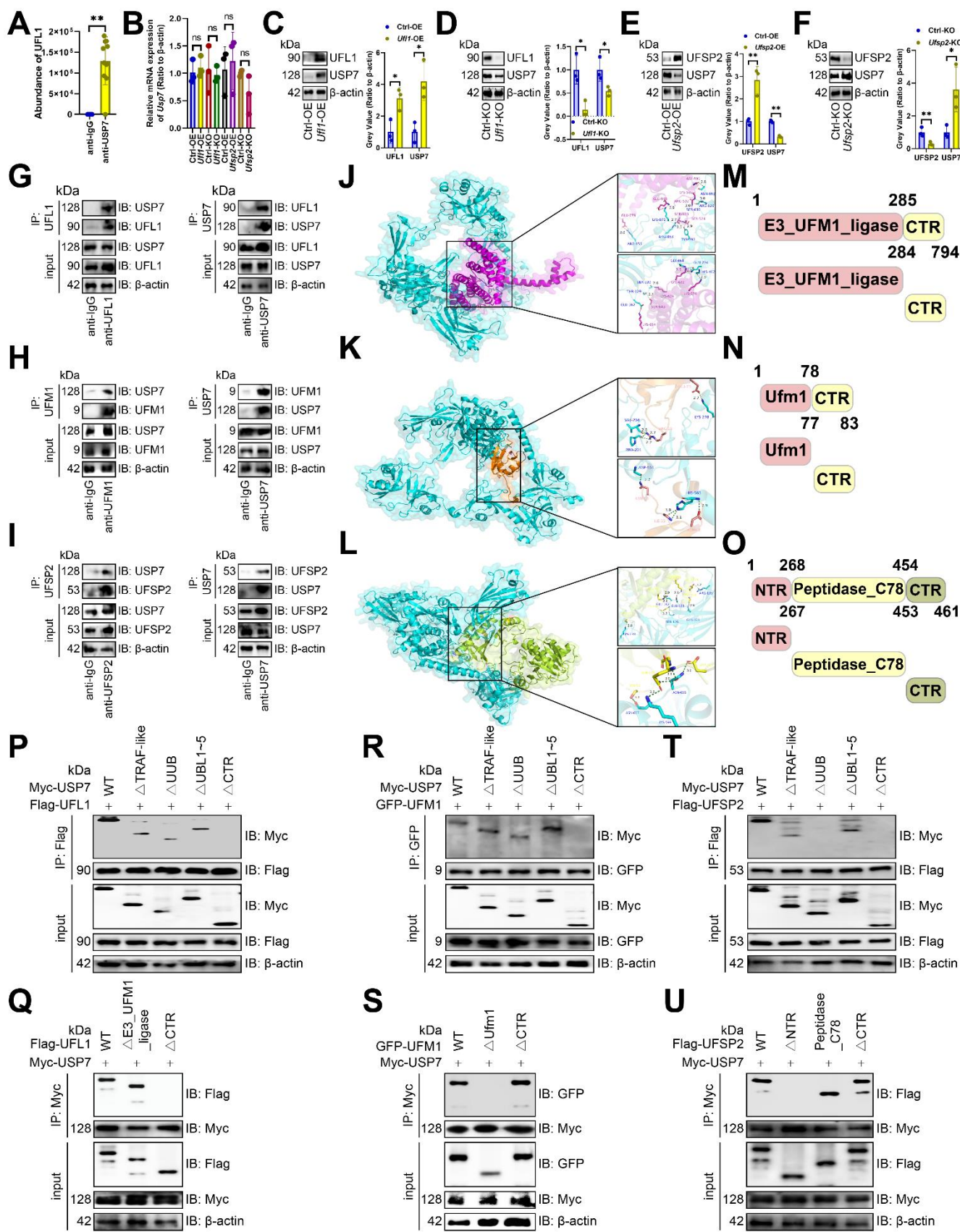


**Figure 6.** USP7 underwent UFMylation. (A) PXD039633 dataset showed the binding of USP7 and UFL1 ( $n = 10$ ). (B) Effects of OE or KO of *Ufl1* or *Ufsp2* on *Usp7* transcript expression in CD3<sup>+</sup> T cells ( $n = 3$ ). (C-F) Effects of OE (C, E) or KO (D, F) of *Ufl1* (C, D) or *Ufsp2* (E, F) on USP7 protein expression in CD3<sup>+</sup> T cells ( $n = 3$ ). (G) CD3<sup>+</sup> T cell lysate was treated with IgG control and UFL1 (left) or USP7 (right) antibodies, and 5% lysate was used as input control ( $n = 3$ ). (H) CD3<sup>+</sup> T cell lysate was treated with anti-IgG controls and -UFM1 (left) or -USP7 (right) antibodies ( $n = 3$ ). (I) CD3<sup>+</sup> T cell lysate was treated with anti-IgG controls and -UFSP2 (left) or -USP7 (right) antibodies ( $n = 3$ ). (J-L) Surface plot presented docking models and interface residues between USP7 (sky blue) and UFL1 (purple) (J)/UFM1 (orange) (K)/UFSP2 (green) (L) proteins, with hydrogen bonds highlighted by dashed lines. (M-O) Schematic plot of the domain-deficient mutants of UFL1 (M), UFM1 (N), and UFSP2 (O). (P, Q) Immunoprecipitation identified key domains of USP7 and UFL1 binding ( $n = 3$ ). CD3<sup>+</sup> T cells were co-transfected with WT or domain-deficient mutants of Flag-labeled UFL1 and Myc-labeled USP7 (P) and vice versa (Q). (R, S) Immunoprecipitation identified key domains of USP7 and UFM1 binding ( $n = 3$ ). CD3<sup>+</sup> T cells were co-transfected with WT or domain-deficient mutants of GFP-labeled UFM1 and Myc-labeled USP7 (R) and vice versa (S). (T, U) Immunoprecipitation identified key domains of USP7 and UFSP2 binding ( $n = 3$ ). CD3<sup>+</sup> T cells were co-transfected with Flag-labeled UFSP2 and Myc-labeled WT or domain-deficient mutants of USP7 (T) and vice versa (U). (A-F) represented mean  $\pm$  SD analyzed by unpaired  $t$  test. \* $P < 0.05$ , \*\* $P < 0.01$ . KO, knockout; OE, overexpression; WT, wild-type.

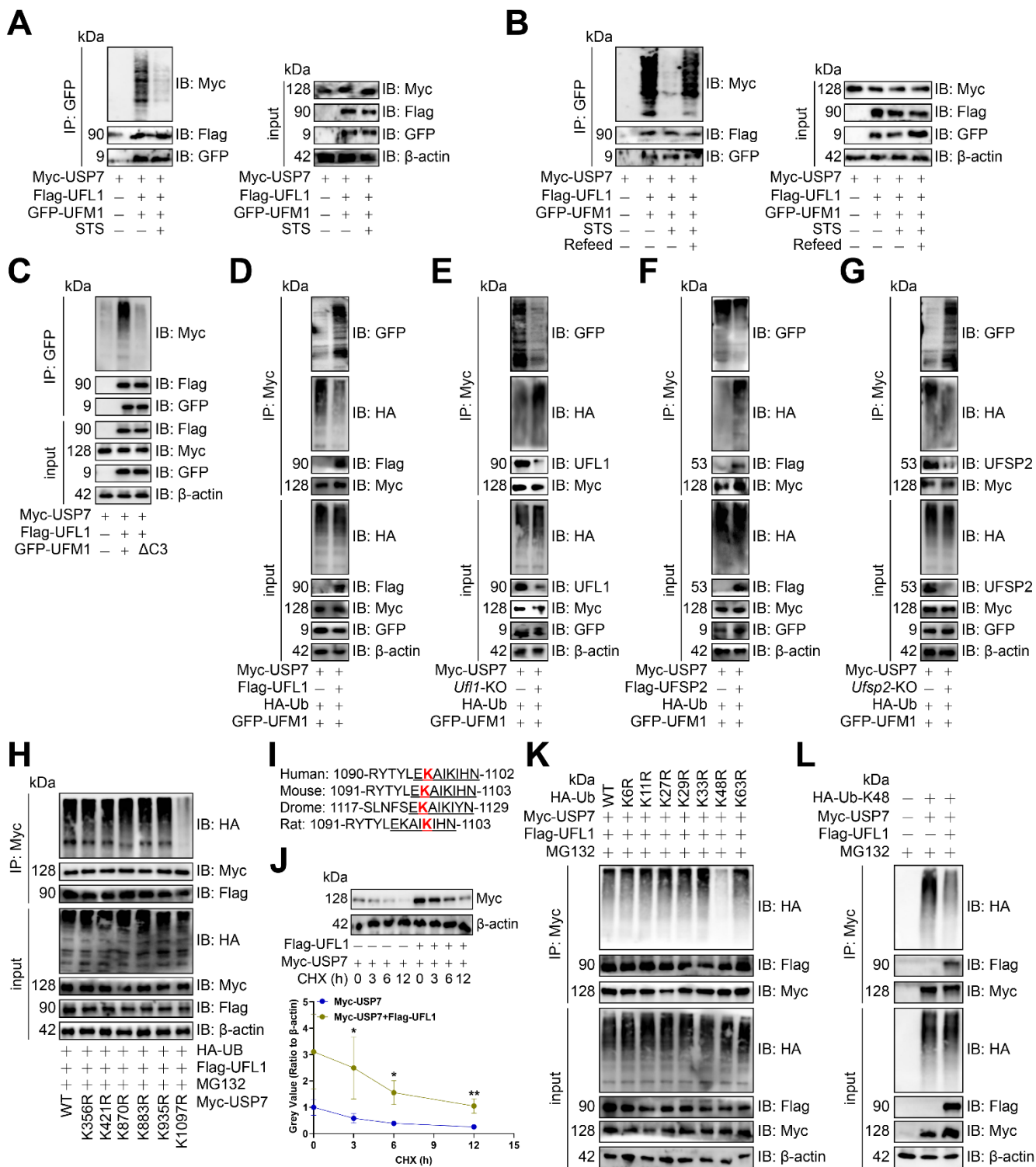
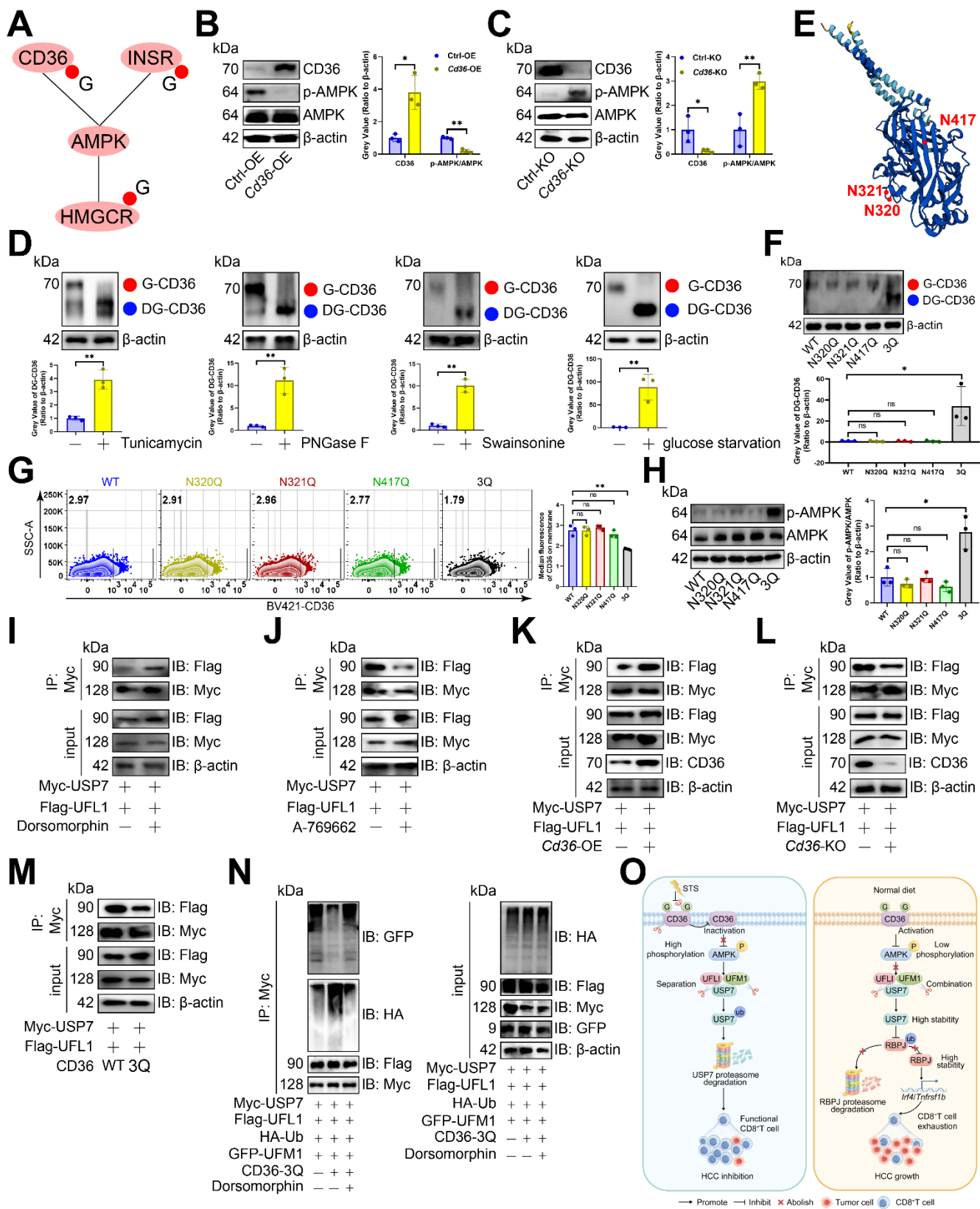


**Figure 7.** STS inhibited USP7 UFMylation thus increasing its ubiquitination. (A-C) Effects of short-term starvation (A), refeed (B), and deletion of the last three amino acid residues (83Gly-Ser-Cys85,  $\Delta$ C3) of UFM1 (C) on USP7 UFMylation ( $n = 3$ ). CD3<sup>+</sup> T cells were co-transfected with Myc-labeled USP7, Flag-labeled UFL1, and GFP-labeled WT or deletion mutants of UFM1. (D-G) Effects of OE

977 (D, F) or KO (E, G) of *Ufl1* (D, E) or *Ufsp2* (F, G) on USP7 UFMylation in CD3<sup>+</sup> T cells ( $n = 3$ ). (H)  
978 Polyubiquitination of six Myc-labeled USP7 lysine mutants in CD3<sup>+</sup> T cells ( $n = 3$ ). (I) Cross-species  
979 conservation of K1097 of USP7. Red indicated lysine site linked to ubiquitin. Underline indicated the  
980 same amino acid sequence. (J) CD3<sup>+</sup> T cells with Myc-labeled USP7 were treated with Cycloheximide  
981 and USP7 protein expression was evaluated by immunoblotting ( $n = 3$ ). (K) Ubiquitination chain  
982 analysis of USP7 in CD3<sup>+</sup> T cells ( $n = 3$ ). (L) Effects of UFL1 on K48-linked USP7 ubiquitination in  
983 CD3<sup>+</sup> T cells ( $n = 3$ ). (J) represented mean  $\pm$  SD analyzed by unpaired  $t$  test. \* $P < 0.05$ , \*\* $P < 0.01$ . KO,  
984 knockout; OE, overexpression; WT, wild-type.





985

986 **Figure 8.** STS inhibited CD36 N-glycosylation and thus preventing USP7 UFMylation. (A) AMPK

987 pathway-associated proteins that might undergo N-glycosylation. (B, C) Effects of OE (B) or KO (C)

988 of *Cd36* on AMPK phosphorylation in CD3<sup>+</sup> T cells ( $n = 3$ ). (D) Effects of Tunicamycin, PNGase F,  
989 Swainsonine, and glucose starvation on CD36 N-glycosylation in CD3<sup>+</sup> T cells ( $n = 3$ ). (E) Protein  
990 structure and N-glycosylation site of CD36. (F) Effects of three possible N-glycosylated asparagine  
991 mutations to glutamine on CD36 expression in CD3<sup>+</sup> T cells ( $n = 3$ ). (G) Influence of mutations of  
992 three N-glycosylation sites on the membrane localization of CD36 on non-permeable CD3<sup>+</sup> T cells ( $n =$   
993 3). (H) Effects of three N-glycosylation site mutations on AMPK phosphorylation in CD3<sup>+</sup> T cells ( $n =$   
994 3). (I-M) Effects of AMPK inhibitor Dorsomorphine (I), AMPK agonist A-769662 (J), *Cd36*-OE (K),  
995 *Cd36*-KO (L), or mutations of three N-glycosylation sites (M) on the binding of USP7 and UFL1 in  
996 CD3<sup>+</sup> T cells ( $n = 3$ ). (N) Influence of mutations of three N-glycosylation sites and Dorsomorphine on  
997 USP7 UFMylation in CD3<sup>+</sup> T cells ( $n = 3$ ). (O) Mechanism diagram. (B-D) and (F-H) represented  
998 mean  $\pm$  SD analyzed by unpaired  $t$  test. \* $P < 0.05$ , \*\* $P < 0.01$ . KO, knockout; OE, overexpression.